EarthArXiv postprint, accepted for publication in the Journal of Structural Geology -
https://doi.org/10.1016/j.jsg.2018.11.009

Slip on wavy frictional faults: is the 3rd dimension a sticking point?

Timothy Davis[1], Eleonora Rivalta[1], David Healy[2]

[1]GFZ (GeoForschungsZentrum), Physics of Earthquakes and Volcanoes, Helmholtzstraße 6/7, Building H 7, 14467 Potsdam. {davis,rivalta}@gfz-potsdam.de, [2]School of Geosciences, King's College, University of Aberdeen, Aberdeen, AB24 3UE, UK {d.healy}@abdn.ac.uk

ABSTRACT

The formulation for the 3D triangular displacement discontinuity boundary element method with frictional constraints is described in detail. Its accuracy in comparison to analytical solutions is then quantified. We show how this can be used to approximate stress intensity factors at the crack tips. Using this method, we go on to quantify how slip is reduced on fault surfaces with topography, where the asperities are approximated as a sinusoidal waveform, i.e. corrugations. We use stress boundary conditions (compressive) orientated such that frictional contacts shear. We show that slip reductions relative to planar faults for 2D line and 3D penny-shaped crack models are comparable within 10% when slip is perpendicular to the corrugations. Using the 3D model, we then show how slip is reduced more when corrugation wavelengths are doubled compared to the reduction due to corrugation alignment with the slip direction. When slip is parallel with the corrugation alignment we show that reducing the out-of-plane stress, from the normal traction acting on the fault when planar to that resolved on a perpendicular plane, has the same effect as halving the length of the corrugation waveform in terms of slip reduction for a given amplitude.

Introduction

Fault slip profiles

Discontinuities within rock masses such as faults are commonly simplified as broadly planar structures, and relative displacement of the fault faces generates deformation in the surrounding rock. The aim of this paper is to assess the degree to which non-planar fault surfaces influence both the slip (fault parallel) and opening (fault normal) displacements for faults oriented such that they slide in the regional stress field. In the geological literature, an early theoretical treatment of discontinuities in the context of Linear Elastic Fracture Mechanics (LEFM) was outlined by Pollard and Segall (1987). Their text supplies analytical solutions for shearing and opening of the faces of a line crack and the resultant stresses and strains induced in the surrounding material. For these solutions, the medium surrounding the discontinuity is treated as a linear elastic material and the resultant deformation is static, satisfying a uniform stress drop prescribed at the fracture surface. The resultant displacement of the faces is such that these are traction free. Despite the many idealisations, the equations in Pollard and Segall (1987) can be used to gain insight into the slip distribution of faults. A quantitative understanding of fault slip profiles is of interest because:

- Fault slip profiles, combined with fault length scaling relationships, can be used to constrain fault displacement on structures where data is sparse (e.g. Kim and Sanderson (2005), e.g. in the subsurface.
- Slip on non-planar faults may promote local opening (or closing) of fault faces, and such movements can impact fault zone permeability, e.g. Figure 4 of Ritz et al. (2015).

Numerical models have shown that several parameters can perturb the slip distributions of fault surfaces away from the simple elliptical profiles described in Pollard and Segall (1987). These are:

- Fault overlap (Crider, 2001; Kattenhorn and Pollard, 2001).

- Fault corrugations (Marshall and Morris, 2012; Ritz and Pollard, 2012; Ritz et al., 2015).
- Fault tip-line shape (Willemse, 1997).
- Non-uniform stresses and friction distributions on the fracture surface (Bürgmann et al., 1994; Cowie and Scholz, 1992).

The focus of this paper is to quantify the effects of non-planar fault surfaces on the slip and opening distributions of isolated faults in three dimensions (3D).

Motivation: non-planar faults

In this study, we use the term 'faults' for surfaces with shear displacement and the term 'fractures' or 'cracks' more generally for surfaces with low offset where both opening and/or shear displacement is observed, these terms are common in LEFM literature. We focus on metre-scale faults to avoid the additional complexities of gravitational stress gradients, inhomogeneous material interfaces, and damage (Ritz et al., 2015). Several mechanisms cause the faces of fractures in rock masses to deviate from planar, these can occur both during initial fracture growth, and later, as slip accumulates on the fault surface. Examples of such mechanisms are:

1. Mixed mode fracture propagation during fracture growth, which introduces relatively cohesionless curved or stepped surfaces into the rock as the fracture tip deviates from a planar path as it grows, this has been shown experimentally (e.g. Cooke and Pollard (1996); Dyskin et al. (2003); Thomas and Pollard (1993) and several numerical criteria exist to evaluate this phenomenon (e.g. Baydoun and Fries (2012); Erdogan and Sih (1963); Lazarus et al. (2008);
2. Fracture growth by linkage of discontinuities, pores, or inclusions (e.g. Davis et al. (2017); Huang et al. (2015); Janeiro and Einstein (2010); Olson and Pollard (1989);
3. Roughening of fault walls during shearing (e.g. Brodsky et al. (2016); Renard et al. (2012)).

4. Non-uniform stresses and friction distributions on the fracture surface (Bürgmann et al., 1994; Cowie and Scholz, 1992).

For all these mechanisms parts of the fracture surface will evolve geometrically as it shears. Relative to the final direction of shearing mechanisms 1) and 2) should introduce complex steps in the fracture that have a spread of orientations relative to the direction of shearing, dependent on the boundary conditions driving growth and on the distribution of initial cracks. Assuming the rock is under compression and that the fracture grows by linkage of wing cracks the final fracture will be stepped with steps that are perpendicular to the final direction of shearing (e.g. Yang et al. (2008). For 3) asperities will be aligned parallel with the shear direction. Note the far field stresses driving shearing of the fractures faces can change over time, relative to the alignment of asperities. It is therefore reasonable to question how deviations from a planar surface affect the evolving fault slip profile as a fault shears and slips. In this study, we idealise fault surface roughness as a smoothly and continuously corrugated sinusoidal waveform. Although this is an oversimplification of the roughness of mm-metre scale fault surfaces, it is a useful end member situation for the evaluation of the effects of roughness (and its orientation), on the resultant slip distributions of faults.

Previous numerical work

The 2D numerical study of Ritz and Pollard (2012) explored how non-planarity affects the resultant slip profiles of fracture surfaces, where non-planarity is modelled as sinusoidal waveforms or 'corrugations'. As the study of Ritz and Pollard (2012) is 2D, fracture walls shear perpendicular to the asperities on the fracture faces. The boundary conditions are set such that the two principal stresses driving shearing are both compressive, and the ratio between these is calculated empirically, based on the observations of shearing pre-cut fractures from Byerlee (1978). Ritz and Pollard (2012) showed that as the asperity wavelength decreases, or its amplitude increases, mean slip is reduced. The slip distribution deviates significantly from that of a planar fault. Greater complexity of asperity geometry was introduced in the study of Dieterich and Smith (2009) where fault plane topography was modelled as random fractal

roughness. This study also models slip on 2D frictional surfaces and the faults satisfy a uniform shear stress drop aligned with the tips of the fault line. The positive shear stress boundary condition used is equivalent to the stress in a body induced by perpendicular inclined tensional and compressional stress of equal magnitude. This boundary condition puts planes of certain orientations into net tension and is unrealistic for a fault under confining crustal conditions. The 3D numerical analysis of Marshall and Morris (2012) examined the net slip for 3D 'frictionless faults' driven by a uniaxial compressive stress, typically 45° to the fault surface. Constraints were imposed such that the fault faces do not interpenetrate but frictional resistance itself was not considered. The study states that total scalar seismic moment release is not significantly different between rough and planar faults, but this contrasts strongly with the findings of the 2D study of Ritz and Pollard (2012), which has more physically realistic boundary conditions and includes friction. Therefore, we surmise that an analysis in 2D alone cannot provide insights into the mechanics of slip along the corrugation direction. The aim of the current study is to extend the comprehensive 2D analysis of Ritz and Pollard (2012) into 3D. We question how the corrugation orientation in relation to the far field stresses affects slip distributions (including openings) of the fault surfaces. Referring to 'in-plane' stresses in our 3D model as those in the plane containing both the faults normal and shear vector direction, we also quantify the effect the 'out-of-plane' stress has on 3D slip distributions. Using similar boundary conditions to Ritz and Pollard (2012), we also quantify the differences between 2D and 3D analyses of such phenomena when corrugations in 3D are also perpendicular to the slip direction.

Background

Theoretical background and terminology

[Figure 1 about here.]

As in the study of Pollard and Segall (1987) this study focuses on faults confined within a linear isotropic elastic

medium. The material can therefore be described by two elastic constants; here we use Poisson's ratio (ν) and the shear modulus (G). For planar 2D and 3D faults loaded by a constant shear traction as shown in 1, these constants are related to slip in the following manner Eshelby (1963); Pollard and Segall (1987):

2D line crack, at $L < a$:

$$D_s = \frac{(1-\nu)t_s}{G}\sqrt{a^2 - L^2}. \tag{1}$$

3D penny-shaped crack, at $L < a$:

$$D_s = \frac{4(1-\nu)at_s}{\pi(2-\nu)G}\sqrt{1 - \frac{L^2}{a^2}}. \tag{2}$$

Eqs. 1 and 2 supply the displacements D_s of the planar cases of a 2D line crack and 3D penny-shaped crack walls loaded by a constant shear traction t_s. Note this is the displacement of one wall of the crack away from its starting position. The result of these equations is that the faces are free of the shear traction imposed due to the resultant slip, note that we ignore tilting of the crack in this study. Here, a is the radius or half-length of the crack and L is the length from the crack centre to an observation point on the crack wall. We use traction in these equations instead of a remote stress driving slip on the crack for two reasons: 1) this removes the dependence on local coordinate systems and relative fracture orientation, and 2) we can directly input friction into these equations without the need for coordinate system transformations. For these equations, both in 2D and 3D, lower values of ν and G cause greater slip of the crack walls. Note that the equations for the opening of a line crack are found by simply replacing t_s by t_n in Eq. 1. For a penny-shaped crack under a tensile stress the opening displacement and its corresponding stress intensity are found using the line crack equations for this boundary condition and multiplying these by $2/\pi$.

Integrating Eq. 1 and applying shell integration to the radially symmetric curve from Eq. 2 between the interval 0 to a we can find the total 'area' (A) or 'volume' (V) of slip of one of the cracks walls. The results are:

2D line crack:

$$A = \frac{\pi(1-\nu)t_s a^2}{2G}. \tag{3}$$

3D penny-shaped crack:

$$V = \frac{8(1-\nu)t_s a^3}{3(2-\nu)G}. \tag{4}$$

Contextually, Eq. 3 is the area under the curve of static slip distributions typically shown for a 2D fracture, e.g. Ritz et al. (2015). These terms can also be converted to seismic moment using:

$$M_0 = V * G \tag{5}$$

Faults buried in the subsurface will be subject to a non-zero confining stress, depending on depth. A proportion of this force resolves as a compressive force directed along the surfaces normal; resolving the force as a traction we adopt the notation t_n. The normal and shear tractions on the surface can be combined with friction to find the resolved shear traction driving slip on the fault surface Pollard and Fletcher (2005):

$$|t_{s\_res}| = |t_s| + \mu t_n - S_f \tag{6}$$

The result of Eq. 6 can be put into Eqs. 1 – 4 to find the slip profile of a fault under crustal stress conditions. Eq. 6 describes the resultant shear traction t_{s_res} on a plane under compression after the frictional properties, the coefficient of friction (μ) and cohesion (S_f), have been considered. The bars surrounding t_s represent the use of absolute values. We adopt a convention where a negative value in t_n represents a compressive force. Note that Eq. 6 ignores the sign and therefore the relative direction of the input t_s.

Motivation

Visual examples of fault roughness show it is ubiquitous but varied e.g. Cann et al. (1997); Griffith et al. (2010); Jones et al. (2009); Ritz et al. (2015); Sagy et al. (2007). Many previous studies of rough fault surfaces have focussed

on the scaling of roughness (Candela et al., 2011; Resor and Meer, 2009). Other studies look at how such corrugations deflect slip, at both kilometre fault scales (Roberts and Ganas, 2000) and locally on the fault surface (Kirkpatrick and Brodsky, 2014). Recent experimental studies have attempted to model how friction changes with the contact area and development of asperities and shear surfaces (e.g., Harbord et al. (2017)). The aim of such studies is to look at how roughness and pressure change the contact area of the asperities and hence the friction. Fracture geometry and roughness also influences fracture stiffness and has been shown experimentally to control nucleation points of slip surface displacement (Choi et al., 2014; Hedayat et al., 2014). Although much of the previous work on rough faults has centred on the roughness itself and the scaling, there has been less work on the mechanics of rough faults, especially in 3D. In this study, a single-scale 'roughness' wavelength is used in each model. This neglects roughness below a certain scale, assuming that small-scale asperities and their contact mechanics can be reduced to the mechanical problem of a planar surface with a uniform coefficient of friction, which is the underlying assumption of Coulomb's friction law (Persson, 2006). This study therefore focuses on how the larger scale geometrical asperities of a surface, in relation to both the remote stresses and the shearing over these irregularities, inhibits or promotes the sliding of faults.

Displacement discontinuity method with friction

In this section, we detail the numerical method used to model sliding surfaces with frictional properties. A frictional adaptation of the displacement discontinuity boundary element method (DDM) is employed. Such adaptations in 3D have been described in previous works (Kaven et al., 2012). For the sake of clarity in notation and in defining a clear convention we describe the matrix system here.

3D DDM formulation: equations, elements and convention

The whole space triangular element formulations of Nikkhoo and Walter (2015) are used as the basic displacement discontinuities in our method. The elements in this publication describe the stress perturbations and displacements

in an isotropic linear elastic medium caused by the face of a planar triangle displacing with a constant mirrored movement. In the method, boundaries are meshed as 3D triangulated surfaces, where each face of the mesh acts as a triangular dislocation. Coefficient matrices $[A]$ are built and a vector is supplied that describes the remote stresses resolved as a traction $[t^{\infty}]$ at each face of the boundary. The displacement discontinuity method in 3D is then solved as:

$$D = -A^{-1}t^{\infty} \tag{7}$$

Expanding Eq. 7 for the 3D DDM method the matrix system is as follows:

$$\begin{bmatrix} D_n^i \\ D_{ss}^i \\ D_{ds}^i \end{bmatrix} = - \begin{bmatrix} A_{D_n t_n}^{ij} & A_{D_{ss} t_n}^{ij} & A_{D_{ds} t_n}^{ij} \\ A_{D_n t_{ss}}^{ij} & A_{D_{ss} t_{ss}}^{ij} & A_{D_{ds} t_{ss}}^{ij} \\ A_{D_n t_{ds}}^{ij} & A_{D_{ss} t_{ds}}^{ij} & A_{D_{ds} t_{ds}}^{ij} \end{bmatrix}^{-1} \begin{bmatrix} t_n^i \\ t_{ss}^i \\ t_{ds}^i \end{bmatrix} \tag{8}$$

[Figure 2 about here.]

In this system, D is a vector containing the movement of each triangles face (i.e. a displacement discontinuity), where subscripts n, ds and ss represent displacement of the faces in the normal, dip-slip, and strike-slip directions respectively. Vector t^{∞} represents the remote stress resolved as a traction on the mid-points (geometric incenter) of each triangular face. The sign of A is flipped as we have adopted the same sign convention for the displacement of discontinuities and direction of traction, summarised in Fig. 2.

For each sub-matrix of square coefficient matrix A in Eqs. 7 and 8, the first subscript D represents the displacement of an element with its direction defined by the lower subscripts. The second subscript t represents the traction in the direction of its respective subscript. For example, $A_{D_n t_{ss}}^{ij}$ is a square matrix that describes how much an opening displacement of one unit length at element j effects the strike-slip shear traction on element i. Each column in this matrix is the effect of one element on the mid-point of every other element.

EarthArXiv postprint, accepted for publication in the Journal of Structural Geology -
https://doi.org/10.1016/j.jsg.2018.11.009

Aims of the DDM solution

In Eqs. 7 and 8, the aim is to find a static slip distribution that approximates the mid-point of each face of the boundary as traction free (t_n, t_{ss} and $t_{ds} = 0$) under the given remote stress defined in the vector t^{∞} on the right-hand side of the equation. Once D is found, DA results in traction vector t^B, which represents the stresses at each mid-point induced by the displacement of the cracks walls. The result of Eq. 7 is that t^B and t^{∞} should oppose each other resulting in a solution where there is no traction at any triangle mid-point along the meshed boundary:

$$\begin{aligned} 0 &= t_n^B + t_n^{\infty} \\ 0 &= t_{ss}^B + t_{ss}^{\infty} \\ 0 &= t_{ds}^B + t_{ds}^{\infty} \end{aligned} \tag{9}$$

DDM formulation with friction

To add frictional constraints to this problem, the system of equations 7 and 8 is reformulated as a linear complementarity problem (Kaven et al., 2012). We use the open source complementarity solver of Niebe and Erleben (2015) implemented in MATLAB. For full details on the accuracy and convergence criterion of the complementarity solver see Niebe and Erleben (2015). For our analysis we have used the default converge criterion of 10 times the numerical precision and the zero Newton equation strategy supplied in the code. Following the notation of Niebe and Erleben (2015) the linear complementarity problem can be stated as:

$$y = ax + b \tag{10}$$

In Eq. 10 x, y, and b are vectors and a is a square matrix. For this problem, the following constraints are set:

$$x \cdot y = 0 \tag{11}$$

$$y \geq 0 \tag{12}$$

$$x \geq 0 \tag{13}$$

In this formulation vectors x and y are unknowns representing tractions and or displacement discontinuities as the solver progresses. They are created such that each pair of corresponding values in the vectors contains a traction and displacement discontinuity and that the sign convention in vector x is flipped. Vector b is filled with the results from Eq. 8, if all displacements are positive according to our convention all constraints are already met, D_n must be positive so the coefficient of friction does not need to be considered. If any displacements in b are negative, then the constraint in Eq. 12 is not met and x will begin to fill with opposing with non-zero values. The expanded form of Eq. 10 for a 3D DDM problem is:

$$\begin{bmatrix} DF_n^{i+} \\ DF_{ss}^{i+} \\ DF_{ds}^{i+} \\ t_{ss}^{i+} \\ t_{ds}^{i+} \end{bmatrix} = \begin{bmatrix} (C^{ij}_{D_n t_n} - (C^{ij}_{D_n t_{ss}} I\mu^i) - (C^{ij}_{D_n t_{ds}} I\mu^i)) & C^{ij}_{D_n t_{ss}} & C^{ij}_{D_n t_{ds}} & 0 & 0 \\ (C^{ij}_{D_{ss} t_n} - (C^{ij}_{D_{ss} t_{ss}} I\mu^i) - (C^{ij}_{D_{ss} t_{ds}} I\mu^i)) & C^{ij}_{D_{ss} t_{ss}} & C^{ij}_{D_{ss} t_{ds}} & I & 0 \\ (C^{ij}_{D_{ds} t_n} - (C^{ij}_{D_{ds} t_{ss}} I\mu^i) - (C^{ij}_{D_{ds} t_{ds}} I\mu^i)) & C^{ij}_{D_{ds} t_{ss}} & C^{ij}_{D_{ds} t_{ds}} & 0 & I \\ 2I\mu^i & -I & 0 & 0 & 0 \\ 2I\mu^i & 0 & -I & 0 & 0 \end{bmatrix} \begin{bmatrix} t_n^{i-} \\ t_{ss}^{i-} \\ t_{ds}^{i-} \\ DF_{ss}^{i-} \\ DF_{ds}^{i-} \end{bmatrix} + \begin{bmatrix} D_n^{i+} - (C^{ij}_{D_n t_{ss}} S_f^i) - (C^{ij}_{D_n t_{ds}} S_f^i) \\ D_{ss}^{i+} - (C^{ij}_{D_{ss} t_{ss}} S_f^i) - (C^{ij}_{D_{ss} t_{ds}} S_f^i)) \\ D_{ds}^{i+} - (C^{ij}_{D_{ds} t_{ss}} S_f^i) - (C^{ij}_{D_{ds} t_{ds}} S_f^i) \\ 2S_f^i \\ 2S_f^i \end{bmatrix} \tag{14}$$

Where:

$$\begin{bmatrix} C^{ij}_{D_n t_n} & C^{ij}_{D_n t_{ss}} & C^{ij}_{D_n t_{ds}} \\ C^{ij}_{D_{ss} t_n} & C^{ij}_{D_{ss} t_{ss}} & C^{ij}_{D_{ss} t_{ds}} \\ C^{ij}_{D_{ds} t_n} & C^{ij}_{D_{ds} t_{ss}} & C^{ij}_{D_{ds} t_{ds}} \end{bmatrix} = - \begin{bmatrix} A^{ij}_{D_n t_n} & A^{ij}_{D_{ss} t_n} & A^{ij}_{D_{ds} t_n} \\ A^{ij}_{D_n t_{ss}} & A^{ij}_{D_{ss} t_{ss}} & A^{ij}_{D_{ds} t_{ss}} \\ A^{ij}_{D_n t_{ds}} & A^{ij}_{D_{ss} t_{ds}} & A^{ij}_{D_{ds} t_{ds}} \end{bmatrix}^{-1} \tag{15}$$

Eq. 14 describes the 3D complementarity equation system for friction on fault surfaces in the 3D DDM method. C is the matrix inverse of the collated coefficient matrix A from Eq. 8; the sub-matrices of C are extracted as in Eq. 15. Matrix C can be described as follows: the summed influence of all elements displacing the amount described in each column of matrix C will cause a traction of one stress unit, t^B on element i in the direction defined by the subscript. The other traction components at this element and all tractions at every other element will be 0. S_f (the cohesive strength of the material) and μ (the coefficient of friction) are defined as vectors, with one value for each element. I is an identity matrix (a square matrix of zeros with ones on the main-diagonal). DF represents the resultant displacement discontinuities when friction is considered. Values of D in vector b (Eq. 14) are the results of Eq. 8. Negative superscripts in Eq. 14 (vector x) are values with the opposite sign to the convention shown in Fig. 2. This means that once solved, positive values in x of Eqs. 10 and 14 must be flipped in sign so the boundary displacements cause stresses that satisfy Eq. 10. The resultant displacement discontinuities at each face are therefore calculated from the results of Eq. 10 as:

$$D = y - x \tag{16}$$

Note, this assumes that the corresponding vectors from x and y are extracted and aligned before this is performed. To stabilise the implementation, matrix conditioning is used. The matrix A in Eq. 15 is scaled by a constant before it is inverted. This constant is the mean value of the half-perimeter length of all the triangles divided by the shear modulus. In the 2D code for line elements we use a similar scaling, the mean element half-length divided by the shear modulus, multiplied by 100. The output element displacements of Eq. 14 are simply multiplied by this scalar value to find the

true displacements. Without this scaling, the solver may fail to converge if both the coordinates and/or driving stresses are not scaled around values close to one. Note that the scaling described here assumes that the elements in the model have similar length scales and shapes.

Aims of the frictional DDM solution

Eqs. 8 and 14 attempt to reach a solution where all elements are free of t_{s_res}, which is the shear traction calculated using Eq. 6, either through shearing or opening of elements. Note that each element only shears if its frictional constraints allow it. The resultant boundary should also be free of tensile tractions defined in vector t^{∞}. This solution explicitly factors in changes in the normal or shear traction and the associated frictional resistance due to the displacement of elements in the result as the solver progresses. In the formulation described, the input mesh represents an infinitesimally thin crack with initially coincident faces. To allow given surfaces to interpenetrate in this formulation an arbitrarily large value bigger than the amount needed to close the fracture in the stress field can be added to D_n for the necessary elements vector b in Eq. 8/14. This value is then subtracted from these elements in the outputs of Eq. 16. An example use case is modelling both fractures and stresses due to topographic loading, such topographic stresses can be modelled with the BEM as described in Martel and Muller (2000) where elements representing the topography must be able to both open and close. This manipulation also allows for the modelling of initially open fractures, the value added to the vector b in this case would be the fractures initial opening profile.

[Figure 3 about here.]

Fig. 3 shows the polygonal frictional approximation as described in Kaven et al. (2012). Fig. 3a) shows a cross section through the 3D friction cone; in 2D this takes a form comparable to the typical failure envelope of a Mohr-Coulomb plot. Both points P and Q are the same distance in y from the grey cone, therefore have the same resultant traction driving shearing. Fig. 3b) shows a) extended to 3D space. In 3D space, the pyramidal approximation is shown by the dotted lines. In this numerical approximation, the elements with shear tractions large enough to plot outside

of the 'pyramid' will displace, rather than those that plot inside the cone. Fig. 3c) shows an end-on view of the cone shown in b). The approximation overestimates friction for any part of vector t_s that passes through the dark grey area between the pyramidal approximation (square) and the isotropic friction cone (circle). It is clear that this is highest at faces where t_{ds} and t_{ss} are equal. For this situation friction is overestimated by 41% Kaven et al. (2012).

Benchmarking and model setup

Boundary conditions and shear profile of the crack

This test of the numerical method uses the same boundary conditions, initial geometry, and sampling as the remainder of the analysis in this study.

[Figure 4 about here.]

[Figure 5 about here.]

[Figure 6 about here.]

Fig. 5 is a comparison of the numerical result to the slip profile of a penny-shaped crack as described by Eq. 2. The geometry of the problem is shown in Fig. 5. The stress convention used puts σ_1 as the least compressive stress. The boundary conditions have been chosen such that in the xy-plane these match the empirically defined boundary conditions of Ritz and Pollard (2012). Here we summarise the motivation behind the chosen boundary conditions in Ritz and Pollard (2012), Byerlee (1978) finds that the maximum friction of rocks in the upper crust (normal stress of up to 200 MPa) occurs when $0.85t_n = t_s$. Maximum friction being the point in experiments when the contact between two separate blocks of material suddenly shears. Using the ratio 0.85 as the coefficient of friction and placing Eq. 9.45 into Eq. 6.55 of Pollard and Fletcher (2005) as the value of ax and rearranging to find the ratio between σ_{xx} and σ_{yy} (treating these as principal stresses by ignoring σ_{xy}) the following equation is found:

$$\frac{\sigma_3}{\sigma_1} = 2\frac{t_s}{t_n}\sqrt{\left(\frac{t_s}{t_n}\right)^2 + 1} + 2\left(\frac{t_s}{t_n}\right)^2 + 1 \tag{17}$$

For a ratio of t_n to t_s of 0.85 this results in a principal stress ratio of 4.68, Eq. 9.45 of Pollard and Fletcher (2005) supplies the angle of these principal stresses away from the fracture plane, 24.8°. The friction coefficient of the fractures face in our model is set to a value less than 0.85, this takes the fracture surface past failure, allowing it to slip in the defined stress field. We orientate the 3D surface so that its normal points along the y-axis, i.e. an extension of a 2D model. Here Θ is set at 24.8° and is the angle of the normal away from σ_3. The results supplied in the rest of the analysis are scaled relative to these analytical solutions so are dimensionless and can be scaled as necessary.

For the modelling the following parameters were used: the fault radius (a) was set to 1 metre and σ_1 and σ_3 were set to -50 MPa and -233.8 MPa respectively, adhering to the ratio defined above. When resolved into Cartesian tensor components with the fault plane oriented as above these are: σ_{xx} = -201.5 MPa, σ_{yy} = -82.3 MPa and σ_{xy} = -70.0 MPa. The shear modulus (G) was set at 12 GPa while the Poisson's ratio (ν) was set to 0.25. The frictional properties were as follows: no cohesive strength was imposed and the dimensionless value of μ was set to 0.6 (Harbord et al., 2017; Pollard and Fletcher, 2005). For these parameters, the maximum slip from Eq. 2 scales with fracture length ($2a$) in a 1:1,000 relationship. Such a scaling lies at the lower end of shear fractures observed in the field (Kim and Sanderson, 2005).

The analytical solution from Eq. 2 is plotted on Fig. 4 with the boundary conditions stated above driving slip. The surface is meshed using a grid of points within a circle on the xz-plane that have a spacing of 1/65 m. Points on this grid 0.02 m from the circles edge were removed and equilateral triangles where added to approximate a smooth outer boundary of the crack, see Fig. 17. The overestimation of the crack shear displacement at the tip region of the fracture is 30% $\pm$ 5% as shown in Fig. 4. Note that the angular dependency of error is dependent on the mesh used. In the subsequent analysis, we plot the relative area (or volume) of slip on the fault surface to indicate how it is reduced by the fault geometry. This can be calculated numerically with the 2D and 3D DDM using:

2D:

$$A = \frac{\sum(2aD_s)}{\sum 2a} \tag{18}$$

3D:

$$V = \frac{\sum(TD_s)}{\sum T} \tag{19}$$

Where A and V are the area and volume of slip of the 2D or 3D fracture, respectively. T in Eq. 19 is the area of each triangles face and a is the half-length of the 2D elements. D_s is the shear displacement calculated at each element. The following equation is used to evaluate the slip decrease on wavy faults from the reference slip observed for a planar penny-shaped crack:

$$\%A\_reduction = (100/A_p)(A_p - A_w) \tag{20}$$

$$\%V\_reduction = (100/V_p)(V_p - V_w) \tag{21}$$

where the subscript p is the slip of a planar fault, i.e. Eq. 3 and 4 and the subscript w that of a wavy fault. Fig. 6 shows diagrammatically the slip distribution for a planar and a wavy fault. Eq. 21 here would describe the volume between the planar and wavy surfaces.

A second test of the accuracy of the numerical setup in 3D is to calculate how well Eq. 19 approximates Eq. 4 when the fault is planar. Using Eq. 21 this results in a value of 1.08%. The error is deemed acceptable for the current analysis as our results look at levels of slip reduction greater than 1%. This gives an insight into the numerical accuracy of results shown later, where the sampling in 3D described above is used. We have also run our 3D analysis for a mesh as described previously but with half the number of triangles to test how sensitive our results are to sampling. Comparing for the waveform where the observed change in volume and stress intensity reductions is steepest (H = 1% of a and

λ = 25%) we see a maximum difference of 1.5% for the stress intensity and volume of slip reductions reported in our results (Fig. 8 to Fig. 12). Our mesh sampling is therefore deemed high enough to provide stable results at the scales of reduction in these properties that we report.

Our last test of accuracy is to use the output slips from Eq. 16 and compute the tractions using Eq. 8. Converting the boundary conditions to tractions and using Eq. 6 we find the analytical resultant traction. Comparing the analytical and numerical tractions at every elements midpoint, the highest error observed is 1E-7% of the analytical value. This is deemed sufficiently accurate in capturing the boundary condition set.

Corrugations were introduced onto the surface using Eq. 22. The resultant undulations are aligned along the z-axis created by moving each triangles corner point by the y value of the prescribed waveform. To orient these corrugations at different angles to the slip sense a rotation of the surface around the y-axis was then applied (Fig. 5b to c).

$$y = H \sin\left(\frac{2\pi x}{\lambda}\right) \tag{22}$$

Where H is the waveform amplitude and λ the wavelength. Note that we have set an upper limit to the waveforms used in this analysis such that the inflection points on the waveforms (where y = 0) are never angled more than 45 degrees away from the x-axis.

Stress intensity approximation

Stress intensity factors approximate stress distributions and magnitudes at distances very close to a fracture's tip. For a 2D fracture (shear or opening) these have been shown to approximate stress distributions at distances of 10% of the fractures half-length from the tip with less than 15% error Pollard and Fletcher (2005); Pollard and Segall (1987). The accuracy of this approximation increases with decreasing distance from the fracture's tip. In 2D the formula for the stress intensity of a line crack subjected to shearing is:

$$K_{II} = ts\sqrt{a/\pi} \tag{23}$$

Following Tada et al. (2000) the formulas for the stress intensity factors around a penny-shaped crack subject to shearing are:

$$\begin{Bmatrix} K_{II} \\ K_{III} \end{Bmatrix} = \begin{Bmatrix} \cos\theta \\ \sin\theta(1-\nu) \end{Bmatrix} \frac{4t_s\sqrt{a/\pi}}{2-\nu} \tag{24}$$

Where Θ is measured from the crack centre and defines the angle between the shear direction and a location on the crack's tip-line, (Fig. 1). The results of the DDM method can be used to approximate the stress intensity factors at a fracture's tip (Olson, 1991). We have followed the method of Olson (1991) but re-derived the formulas using the equations for a 3D penny-shaped crack (Appendix). The 3D formulas are:

$$\begin{Bmatrix} K_I \\ K_{II} \\ K_{III} \end{Bmatrix} = \begin{Bmatrix} D_n \\ D_{II} \\ D_{III}(1-\nu) \end{Bmatrix} \frac{\sqrt{\pi}G}{\sqrt{h}(1-\nu)2}c \tag{25}$$

In these equations, h is the distance from the mid-point (geometric incenter) of the boundary element to the fracture's tip Ritz et al. (2012), D_n is the normal displacement of this element, D_{II} is the displacement perpendicular to the crack edge, and D_{III} is the displacement parallel with the edge. The correction factor c is used to correct for the errors due to the numerical approximation. This is set to 1/1.834. See the appendix for the reasoning.

[Figure 7 about here.]

The accuracy of the 3D DDM in matching Eq. 24 is shown in Fig. 7. The maximum vertical separation between the analytical curve and points (residual) shown in Fig. 7 is 0.032 for K_{II} and 0.035 for K_{III}, this is for the surface as described in the benchmarking section.

Model results

Effect of corrugation amplitude and wavelength: comparison to 2D results

We now compare the slip reduction differences for 2D and 3D geometries with the same shaped corrugations. The results of Eqs. 20 and 21 are plotted to compare the slip area or volume reduction relative to a planar fault. The fault in 3D is oriented as in Fig. 5b. For this configuration, the 'out-of-plane stress' σ_{zz} in 3D makes no difference to the results as this is not resolved as a traction at any point on the surface.

[Figure 8 about here.]

Fig. 8 shows a comparison between the results for 2D and 3D wavy faults with several amplitudes and four different wavelengths. The 2D sampling has been set to 1,000 equally spaced elements on the fault plane in the x-axis before the waveform is introduced. Slip reductions relative to a planar penny-shaped and line cracks are plotted in Fig. 8 as a function of the surface waveform, and both 2D and 3D results are shown. This shows the simple trends observed in previous 2D studies where resultant slip is reduced by corrugations with higher amplitudes and/or shorter wavelengths (Ritz and Pollard, 2012).

Trends, due to both changes in amplitude (H) and wavelength (λ), in the reduction in slip are similar for the 2D and 3D results. The largest difference between 2D and 3D reductions in slip due to corrugations is less than 10%. Some notable differences are that the 2D results have greater reductions in slip for all modelled wavelengths, except for when the wavelength is larger than the fault half-length (in this case the opposite is true). As the numerical accuracy of the DDM has been quantified as accurate to approximately 1%, the difference between the two results is due to the shape and area of the crack in 3D and the lack of the plane strain boundary condition. From these results, we suggest that the slip distribution profiles documented by Ritz and Pollard (2012) for 2D fractures can be extrapolated to 3D penny-shaped fractures when shearing is perpendicular to the alignment of asperities.

Effect of corrugation orientation in 3D

In this section, we explore the effects of corrugation orientation in relation to the direction of shearing, i.e. changing from the geometry shown in Fig. 5b to that in Fig. 5c. When corrugations are oriented as in Fig. 5c this means σ_{zz} is resolved as a normal traction on some parts of the surface. We start by exploring the changes in slip volume when σ_{zz} is set to the same magnitude as the stress component, σ_{xx}; this is t_n acting on the plane if it was perpendicular to its orientation shown in Fig. 5a. Changes in the magnitude of σ_{zz} are explored later.

Fig. 9 is an example that shows the shearing of a faults faces for the geometries in Fig. 5b and Fig. 5c. An important observation from this figure is that there is no slip in the z direction. The lines running parallel with the x-axis are not perturbed. This is different to the findings of Marshall and Morris (2012) where deviations in slip vector rake are analysed on frictionless faults. For high values of friction and for these boundary conditions the fault plane only slips in directions parallel to the greatest resolved shear traction vector.

[Figure 9 about here.]

[Figure 10 about here.]

Fig. 10 has the same axes and plots the same corrugation waveforms as Fig. 8 but compares slip reductions when corrugations are parallel and perpendicular to the slip direction (Fig. 5b to c). Reviewing the trends in this graph shows that:

- The range in slip reduction due to doubling the wavelengths of corrugations (vertical distance between lines with the same symbol) is almost always greater than the reduction due to corrugation misalignment for a given corrugation waveform (vertical extent of each shaded patch).
- Faults with shorter corrugation wavelengths are more sensitive to corrugation angle relative to slip. These have greater ranges in slip as the corrugation directions change from parallel to perpendicular in relation to the plane

containing the most compressive stress.

[Figure 11 about here.]

Fig. 11 explores what the out-of-plane stress (here σ_{zz}) does to the results of Fig. 10. Two cases are shown: a) σ_{zz} is set equal to σ_{xx}; b) σ_{zz} is equal to σ_{yy} (i.e. t_n when planar). The figure shows slip reductions when corrugations are parallel with the slip direction. For cases when σ_{zz} is reduced so is the additional frictional resistance which allows the fault to slip a greater amount. Here it can be seen that doubling the wavelength of the corrugations (vertical distance between lines with the same symbol) has close to the same effect in reducing slip as decreasing the out-of-plane stress σ_{zz} to the magnitude of the lowest stress driving slip (vertical extent of each shaded patch). Adjusted coefficients of friction are supplied for planar faults in Fig. 11 to give an idea of how this parameter reduces slip volume in comparison to the reductions due to fault waveform. Note these values also apply to Fig. 8 and Fig. 10 also. This gives some idea of the 'effective' friction that would be calculated by fitting a planar fault model to slip data from a wavy fault surface that was subject to the boundary conditions we have described.

Stress intensity factors

Reductions in stress intensity between the 2D and 3D results are shown in Fig. 12. This figure plots results relative to the result from Eq. 24. Note that the 3D results plot the maximum stress intensity on the crack edge. Unlike in Fig. 8 the trends between 2D and 3D results are quite disparate, <40% in places. This is due to the crack tip in 2D being a single point. Fig. 9 shows that parts of the fault surface slip less due to the waveform of the fault surface and its relation to the principal stresses. In 2D if the crack tip is at a location where the slip is reduced then so is the stress intensity. In 3D, the crack has a tip-line so even if slip along parts of its tip-line are reduced, locations along parts of the tip-line in 'releasing bends' will continue to slip. This results in some edges of the fault maintaining higher stress intensities. Note that reductions in K_{III} for the 3D case follow very similar trends to that of K_{II}. This observation

highlights the need for careful consideration of geometry and local departures from the general trends when analysing the results of the previous graphs, Fig. 8, Fig. 10, and Fig. 11.

[Figure 12 about here.]

Effect of waveform on opening aperture

This part of the study focuses on the 'lenticular' openings as described by Ritz et al. (2015). The same basic boundary conditions and constants are used as before, but with an additional pore pressure inside the fracture. In this part of the study a 2D plane strain code is used to model slip perpendicular to the asperity direction. In the 2D study of Ritz and Pollard (2012) a ratio a/λ greater than 11 (when λ is less than 9% of a) was required before opening was observed on parts of the fractures face. We look at openings for faults with longer corrugation wavelengths when there is a pore pressure (P) acting to reduce the effective normal stress confining the surface. From Eq. 6 we can state that increases in pore pressure should increase the overall slip on the fracture surface, this should also promote opening of the surfaces faces:

2D line, at $L < a$:

$$D_n = \frac{2(1-\nu)P}{G}\sqrt{a^2 - L^2} \tag{26}$$

We choose to scale the maximum apertures observed on the wavy faults, so they are relative to the maximum opening observed for a planar line shaped crack dilating due to an internal pressure, (Eq. 26). D_n here being the total separation between the faces not just the displacements of one wall of the crack. Note that the maximum opening here is found by simply setting the term L inside the square root to zero, i.e. the centre of the crack (Fig. 1). This allows us to scale our results to a problem that uses both the same elastic constants and has the same surface geometry (when planar) making our results dimensionless. The internal pressure opening the crack is set to half the magnitude of the normal stress that confines our shear fault when it is planar. In terms of pressure this is a value P, 41.15 MPa.

[Figure 13 about here.]

Fig. 13 shows how openings on the fracture surface change as a function of the waveform of the fracture. The two axes show the parameters that control the waveform and the coloured squares are openings as a percentage of Eq. 12. Note that the dashed lines shown are where waveform slopes are deemed excessive. The graph shows that lenticular openings on confined shear fractures can reach up to 25% of the maximum apertures of an unconfined pressurised crack. Maximal openings are found for waveforms with ratios of λ/H of around 15. Such a ratio and the opening magnitudes will change with friction, pore pressure and driving stresses.

Discussion

Relationships in slip reduction

From the modelling results, the following statements can be made:

1. When slip is perpendicular to the corrugations, results from 2D studies match closely with 3D results (Fig. 8). This suggests that the slip reductions due to the shape of corrugations are not greatly affected by the tip-line shape of the fracture so plane strain (2D) modelling is adequate in this case.

2. When slip is parallel to corrugations, reductions due to doubling corrugation wavelength are greater than the slip reduction due to rotation of the corrugations out of alignment with the slip direction (Fig. 10). This is provided that the out-of-plane stress is high, high being the value of t_n resolved on the crack face when planar.

3. For slip parallel with corrugations, the maximum reduction in slip when changing the out-of-plane stress from low to high matches the reduction in slip when halving the corrugation wavelength. Low here being the value of t_n resolved on a planar crack orientated perpendicular to the crack in our setup (with its normal in the xy-plane).

EarthArXiv postprint, accepted for publication in the Journal of Structural Geology -
https://doi.org/10.1016/j.jsg.2018.11.009

These results should give some indication as to which fault shapes will preferentially accrue more slip in a given slip direction. Such results rely on both an estimation of fault roughness at a larger scale and the stresses driving failure. Note the two latter relationships detailed here are dependent on the coefficient of friction being at 0.6. We have tested if these statements hold true for values of μ between 0.4 – 0.67. Statements 1 and 3 hold true between these values. Statement 2 is still valid when μ is higher, i.e. 0.67, but begins to break down for lower values i.e. 0.4. Here results for the different wavelengths would begin to overlap in Fig. 10. It is worth reviewing the statements earlier that friction is overestimated by 41% on faces where the two shear traction components (t_{ds} and t_{ss}) are of equal magnitude. We can therefore state that trends for the slip parallel with corrugations in Fig. 10 and Fig. 11 will show greater reductions due to friction than would be observed if we modelled this using an isotropic friction cone.

Additional complexity

In 2D the correlation between slip reduction and stress intensity is clear; see Fig. 8 and Fig. 12. This breaks down in 3D where high stress intensities remain even when the total volume of slip is significantly reduced. Similar examples of local departures from the global trend of slip on the fault surface were presented by Ritz and Pollard (2012); here we have shown an example where 3D geometry also introduces such a complexity. Changing the start location and sign of the waveform (phase shift) for faults with longer corrugation wavelengths changes the slip distributions Ritz and Pollard (2012). Changing these parameters will only have substantial effects on slip reductions for corrugations of longer wavelengths, for example the greatest slip reduction shown for the longest wavelength in Fig. 8 increases by up to 10% for a waveform shifted positively by 90 degrees. The other wavelengths modelled here are broadly unaffected (less than 5%).

[Figure 14 about here.]

An obvious question related to the results shown here is how well does the approximation of a smoothly undulating roughness compare to slip on surfaces with real fracture surface roughness? To give some indication of the limitations

of the approximation adopted here, we numerically simulate slip on two more complex geometries to quantify how slip is reduced on such surfaces. We have found slip distributions relative to planar faults for 2D and 3D fracture surface geometries observed in the field. The first is from Ritz et al. (2015) and the second an exposed fracture face on a sandstone outcrop reconstructed using 3D photogrammetry. The sampling of this face is such that roughness below a 10th of the half-length is not captured and additional artefacts may have been introduced during processing. Fig. 14 also shows approximations of these two fractures with waveforms. For the 2D results for the surface shown in Fig. 14 we observe a slip reduction of 17% compared to planar. This compares well to that for the waveform approximation shown, that has an approximate slip reduction of 12% (Fig. 8). For the 3D fracture surface, the slip reduction is 25%. For the approximate waveform from Fig. 10 the slip reduction is 5%. Therefore, for the two surfaces shown here the results suggest that first order approximation will overestimate the volume of slip compared with a natural fracture shape that has multiple length scales of asperities. Intuitively, this will be especially apparent when 3D surface roughness is close to isotropic, i.e. lacking alignment of the asperities. This is seen for small faults (slip<1 m), which in general are characterised by roughness that is closer to isotropic than larger faults ($\sim$10-100 m slip) (Sagy et al., 2007). Power and Durham (1997) show that roughness on fracture surfaces of both natural and experimental tensile fractures is close to isotropic, at scales of 0.001 to 2 cm. To provide a conflicting example, Pollard et al. (2004) show clear examples of joint surfaces with clear anisotropic roughness perpendicular to the fracture tip lines, on the scale of cm's, formed during mixed mode fracture propagation.

We have provided some potential mechanisms that create or cause non-planarity of fractures. None of these mechanisms create the sinusoidal structures observed on some fault surfaces, that are typically above the metre scale (Brodsky et al., 2016; Resor and Meer, 2009). Are our results applicable to such structures? Our model results can be scaled up to a larger scale using the appropriate values in the analytical solutions provided. This is dependent on the assumption that the roughness is not destroyed or modified during slip and that the boundary conditions we have used are still suitable.

Fluid flow

We have quantified the opening of apertures when wavy fault surfaces shear at fluid pressures close to hydrostatic conditions. These open even when confined by remote stresses driving shearing. This is contrary to the assumption that fluid pressure must exceed the normal stress acting on a fracture face before openings are observed (e.g. Mildren et al. (2002)). Fig. 13 uses internal pressure as the variable controlling opening of the fracture. To use the data presented in this figure the input pressure must be scaled so there are reasonable values for the remote stresses that drive shearing. Using the elastic parameters and stresses described previously this suggests that a 10 m-long shear fracture with the correct waveform could have had 1.25 cm lenticular openings. It is of interest to know if in a laboratory, an experiment using pre-cut rock samples would also show increases in the permeability during shear loading, for certain cut shapes.

Conclusions

We have quantified the amount that slip is reduced by friction on 3D fault surfaces with variations in fault topography. We use a first order approximation where topography is modelled as a sinusoidal waveform, i.e. parallel corrugations. Firstly, when typical friction values are considered the fault plane only slips in directions parallel to the resolved traction vector, independent of its direction in relation to the corrugation alignment. Slip reductions due to corrugations are comparable for both 2D line cracks and 3D penny-shaped cracks when shearing is perpendicular to corrugation alignment. Differences in slip reductions when the slip is aligned and misaligned with corrugations appear to be less than the differences in slip reductions when the corrugation wavelength is doubled, when the out-of-plane stresses are high. When the slip vector is aligned with the corrugations on the fault surface, halving the corrugation wavelength has almost the same effect at reducing slip volume as increasing the out-of-plane stress from close to the lowest stress in the plane of shearing up until it matches the normal stress acting on the plane. For lenticular openings on fault surfaces we have quantified which waveforms have the greatest openings: for typical shearing conditions, this

is a λ/H ratio of around 15. Note that opening apertures are observed even when the internal pore fluid pressure does not exceed the remote stresses clamping the fault surface.

Acknowledgements

We thank both reviewers for the constructive reviews which resulted in improvements to the manuscript, the editor Cees Passchier and lastly, Lydia Jagger who helped improve the language of the initial draft. The work here was funded through the Deutsche Forschungsgemeinschaft / International Continental Scientific Drilling Program, grant agreement N. RI 2782/3-1.

Supplementary material

- MATLAB script containing Eq.(1), (2), (3), (4), (5), (23), (24) and (26). 'AppendixEqs.m'
- Text file containing data of triangulation used in numerical analysis. 'Triangulation.csv'
- MATLAB scripts containing the DDM code used in this research can be found at: `https://github.com/Timmmdavis/CutAndDisplace`

Appendix

The aim of this section is to detail how we derive the equations for the stress intensity approximation using the 3D displacement discontinuity method. This allows us to provide reasons for the error in the equation and propose a value to correct for this. We then go on to detail the errors for different meshes types and refinements. It is of note to add that other formulations exist for approximating stresses at a cracks tips using the BEM DDM method, these are either directly calculating stress distributions around the tip or using more complex discontinuities on the

crack edge (Li et al., 2001; Meng et al., 2013). The method of Meng et al. (2013) lacks propagation criterion that are related to measurable fracture strengths of materials but could be adapted for this, the method of Li et al. (2001) directly calculates K_I but has does not detail how to work with shear fractures. Sheibani et al. (2013) describe a similar method to described here for rectangular dislocation elements in 3D, we go into greater detail, deriving the formulas in 3D to show these are the same as 2D, this derivation allows us to correctly identify the sources of error and appropriately adjust for these. We then quantify the accuracy of our approximation. Tada et al. (2000) supply stress intensity factors for 3D penny-shaped cracks loaded by remote stresses:

$$K_I = 2t_n\sqrt{a/\pi} \tag{27}$$

$$\begin{Bmatrix} K_{II} \\ K_{III} \end{Bmatrix} = \begin{Bmatrix} \cos\theta \\ \sin\theta(1-\nu) \end{Bmatrix} \frac{4t_s\sqrt{a/\pi}}{2-\nu} \tag{28}$$

And Eshelby (1963) gives the separation distance between the walls of the crack (penny):

$$D_n = \frac{4a(1-\nu)t_n}{\pi G}\sqrt{1-\frac{L^2}{a^2}} \tag{29}$$

$$D_s = \frac{8a(1-\nu)t_s}{\pi G(2-\nu)}\sqrt{1-\frac{L^2}{a^2}} \tag{30}$$

Rearranging these to give this in terms of traction:

$$D_n\frac{1}{\sqrt{1-\frac{L^2}{a^2}}}\frac{\pi G}{4a(1-\nu)} = t_n \tag{31}$$

$$D_s\frac{1}{\sqrt{1-\frac{L^2}{a^2}}}\frac{\pi G(2-\nu)}{8a(1-\nu)} = t_s \tag{32}$$

Combining Eq. 27,28 with Eq. 31,32, note D_{III} the displacement vector parallel to the crack edge and D_{II} is perpendicular to this, in the plane of the crack. This removes the dependence on Θ in Eq. 28.

$$K_I = D_n \frac{1}{\sqrt{1-\frac{L^2}{a^2}}} \frac{2\sqrt{a/\pi}\pi G}{4a(1-\nu)} \tag{33}$$

$$\begin{Bmatrix} K_{II} \\ K_{III} \end{Bmatrix} = \begin{Bmatrix} D_{II} \\ D_{III}(1-\nu) \end{Bmatrix} \frac{1}{\sqrt{1-\frac{L^2}{a^2}}} \frac{4\sqrt{a/\pi}\pi G(2-\nu)}{(2-\nu)8a(1-\nu)} \tag{34}$$

As the crack tip is approached the reciprocal term goes to zero. Assuming sufficient sampling of the crack so the edge elements are close to the tip we therefore drop this term.

$$K_I = D_n \frac{2\sqrt{a/\pi}\pi G}{4a(1-\nu)} \tag{35}$$

$$\begin{Bmatrix} K_{II} \\ K_{III} \end{Bmatrix} = \begin{Bmatrix} D_{II} \\ D_{III}(1-\nu) \end{Bmatrix} \frac{4\sqrt{a/\pi}\pi G(2-\nu)}{(2-\nu)8a(1-\nu)} \tag{36}$$

After some rearrangement:

$$\begin{Bmatrix} K_I \\ K_{II} \\ K_{III} \end{Bmatrix} = \begin{Bmatrix} D_n \\ D_{II} \\ D_{III}(1-\nu) \end{Bmatrix} \frac{\sqrt{a}\sqrt{\pi}G}{a(1-\nu)2} \tag{37}$$

As $\sqrt(x)/x = 1/\sqrt(x)$ then:

$$\begin{Bmatrix} K_I \\ K_{II} \\ K_{III} \end{Bmatrix} = \begin{Bmatrix} D_n \\ D_{II} \\ D_{III}(1-\nu) \end{Bmatrix} \frac{\sqrt{\pi}G}{\sqrt{a}(1-\nu)2} \tag{38}$$

The BEM DDM method supplies displacements on the crack wall. If h is substituted for a in Eq.38 we simulate a smaller crack with the same opening as the crack tip element close to the fractures tip. Such a crack will have a similar opening profile very close to the tip, i.e. Fig. 15 and therefore a similar stress intensity. This approximation means the terms that specify the crack size in the equations is dropped. Constant c is also added which can be used to correct for the mismatch between the approximation and the analytical solution.

$$\begin{Bmatrix} K_I \\ K_{II} \\ K_{III} \end{Bmatrix} = \begin{Bmatrix} D_n \\ D_{II} \\ D_{III}(1-\nu) \end{Bmatrix} \frac{\sqrt{\pi}G}{\sqrt{h}(1-\nu)2} c \tag{39}$$

[Figure 15 about here.]

The correction factor c therefore adjusts for error in the approximation detailed above, the fact we drop the reciprocal term when deriving the equations, and that due to the overestimation of crack wall displacements from the BEM-DDM method. Fig. 4 shows that the error due to the overestimation of crack wall displacements is 30% $\pm$5%, this error is similar for opening displacements. This overestimation is close to being independent of mesh refinement which can be seen when we compute the accuracy of the approximation. Using analytical formulas, we compute one source of error. Comparing stress intensities for cracks under the same boundary conditions between a crack where a=1 using Eqs. 27 and 28 to the results of Eq. 39 using a displacement of a crack where a is a 1000th of the width with its max displacement defined by the crack wall displacement of the larger crack (Eqs. 29 and 30). The overestimation

of the approximation of Eq. 39 is 41.4%. Combining the two errors the total error of the numerical method is 183.4%. The correction factor is therefore simply 1/1.834.

[Figure 16 about here.]

[Figure 17 about here.]

Fig.16 shows the error due to the stress intensity approximation described, this is compared to the analytical formula for an inclined crack subject to tension described in Tada et al. (2000). We have tested different crack geometries: with normals between 5 and 85 degrees away from z, and the errors for each angle are coincident provided the mesh is the same. The figure shows the results of different meshes, triangulated uniform grids (with an edge of equilateral triangles added) like used in this study and unstructured meshes from the code DistMesh (Persson and Strang, 2004). Note that for both cases we have set a constraint that all the edge triangles are isosceles, see Fig. 17 for examples. The results show the error is relatively stable, with the mean values (shapes) below 4% of the maximum analytical value of each stress intensity. Structured meshes appear to have slightly higher errors, even though for these meshes we have put equilateral triangles around the crack edge. The scatter in the crack tip error as shown in Fig. 4 must therefore be larger for such meshes. For the unstructured meshes the number of triangles (numbers above each data point) increases mean mesh quality, there is a trend for K_{II} and K_{III} where mesh density increases the mean accuracy, but the error is only halved as the mesh size is squared. It must be noted that ν changes the scatter of the crack tip element slip distribution error in shown in Figure 4. This only affects the slip profile estimation of the DDM, for opening this scatter is constant, around 3% for the mesh used in our analysis. For a ν of 0.01 the shear component scatter drops from around 5% to 2% and when increased to 0.49 it is close to 10%. These errors are for the mesh we have used in the rest of the analysis. This change in the scatter with ν in turn affects the error of the stress intensity approximation of K_{II} and K_{III}. In this section we have detailed a method to approximate stress intensities at a fractures tip in 3D where the fracture can have frictional constraints. The method to calculate stress intensities is simple to implement in BEM

DDM formulations or in other methods provided the crack opening/slip profile can be estimated. After correcting for the error of the approximation we have described the error in the stress intensities from using this method. This is caused by scatter in the methods estimation of crack tip displacements. Methods to improve the consistency of the crack opening/slip profile near to the tips have potential to reduce this error.

References

Baydoun, M. and Fries, T. (2012). Crack propagation criteria in three dimensions using the xfem and an explicit–implicit crack description. *International journal of fracture*, 178(1-2):51–70.

Brodsky, E. E., Kirkpatrick, J. D., and Candela, T. (2016). Constraints from fault roughness on the scale-dependent strength of rocks. *Geology*, 44(1):19–22.

Bürgmann, R., Pollard, D. D., and Martel, S. J. (1994). Slip distributions on faults: effects of stress gradients, inelastic deformation, heterogeneous host-rock stiffness, and fault interaction. *Journal of Structural Geology*, 16(12):1675–1690.

Byerlee, J. (1978). Friction of rocks. In *Rock friction and earthquake prediction*, pages 615–626. Springer.

Candela, T., Renard, F., Schmittbuhl, J., Bouchon, M., and Brodsky, E. E. (2011). Fault slip distribution and fault roughness. *Geophysical Journal International*, 187(2):959–968.

Cann, J., Blackman, D., Smith, D., McAllister, E., Janssen, B., Mello, S., Avgerinos, E., Pascoe, A., and Escartin, J. (1997). Corrugated slip surfaces formed at ridge–transform intersections on the mid-atlantic ridge. *Nature*, 385(6614):329–332.

Choi, M.-K., Bobet, A., and Pyrak-Nolte, L. J. (2014). The effect of surface roughness and mixed-mode loading on the stiffness ratio κ x/κ z for fractures. *Geophysics*, 79(5):D319–D331.

Cooke, M. L. and Pollard, D. D. (1996). Fracture propagation paths under mixed mode loading within rectangular blocks of polymethyl methacrylate. *Journal of Geophysical Research: Solid Earth*, 101(B2):3387–3400.

Cowie, P. A. and Scholz, C. H. (1992). Physical explanation for displacement-length relationship of faults using a post-yield fracture mechanics model. *Journal of Structural Geology*, 14:1133–1133.

Crider, J. G. (2001). Oblique slip and the geometry of normal-fault linkage: mechanics and a case study from the basin and range in oregon. *Journal of Structural Geology*, 23(12):1997–2009.

Davis, T., Healy, D., Bubeck, A., and Walker, R. (2017). Stress concentrations around voids in three dimensions: The roots of failure. *Journal of Structural Geology*, 102:193–207.

Dieterich, J. H. and Smith, D. E. (2009). Nonplanar faults: Mechanics of slip and off-fault damage. In *Mechanics, structure and evolution of fault zones*, pages 1799–1815. Springer.

Dyskin, A., Sahouryeh, E., Jewell, R., Joer, H., and Ustinov, K. (2003). Influence of shape and locations of initial 3-d cracks on their growth in uniaxial compression. *Engineering Fracture Mechanics*, 70(15):2115–2136.

Erdogan, F. and Sih, G. (1963). On the crack extension in plates under plane loading and transverse shear.

Eshelby, J. (1963). The distribution of dislocations in an elliptical glide zone. *physica status solidi (b)*, 3(11):2057–2060.

Griffith, W. A., Nielsen, S., Di Toro, G., and Smith, S. A. (2010). Rough faults, distributed weakening, and off-fault deformation. *Journal of Geophysical Research: Solid Earth*, 115(B8).

Harbord, C. W., Nielsen, S. B., De Paola, N., and Holdsworth, R. E. (2017). Earthquake nucleation on rough faults. *Geology*, 45(10):931–934.

Hedayat, A., Pyrak-Nolte, L. J., and Bobet, A. (2014). Multi-modal monitoring of slip along frictional discontinuities. *Rock mechanics and rock engineering*, 47(5):1575–1587.

Huang, Y., Yang, Z., Ren, W., Liu, G., and Zhang, C. (2015). 3d meso-scale fracture modelling and validation of concrete based on in-situ x-ray computed tomography images using damage plasticity model. *International Journal of Solids and Structures*, 67:340–352.

Janeiro, R. P. and Einstein, H. H. (2010). Experimental study of the cracking behavior of specimens containing

inclusions (under uniaxial compression). *International Journal of Fracture*, 164(1):83–102.

Jones, R., Kokkalas, S., and McCaffrey, K. (2009). Quantitative analysis and visualization of nonplanar fault surfaces using terrestrial laser scanning (lidar)—the arkitsa fault, central greece, as a case study. *Geosphere*, 5(6):465–482.

Kattenhorn, S. A. and Pollard, D. D. (2001). Integrating 3-d seismic data, field analogs, and mechanical models in the analysis of segmented normal faults in the wytch farm oil field, southern england, united kingdom. *AAPG bulletin*, 85(7):1183–1210.

Kaven, J. O., Hickman, S. H., Davatzes, N. C., and Mutlu, O. (2012). Linear complementarity formulation for 3d frictional sliding problems. *Computational Geosciences*, 16(3):613–624.

Kim, Y.-S. and Sanderson, D. J. (2005). The relationship between displacement and length of faults: a review. *Earth-Science Reviews*, 68(3-4):317–334.

Kirkpatrick, J. D. and Brodsky, E. E. (2014). Slickenline orientations as a record of fault rock rheology. *Earth and Planetary Science Letters*, 408:24–34.

Lazarus, V., Buchholz, F.-G., Fulland, M., and Wiebesiek, J. (2008). Comparison of predictions by mode ii or mode iii criteria on crack front twisting in three or four point bending experiments. *International journal of fracture*, 153(2):141–151.

Li, H., Liu, C., Mizuta, Y., and Kayupov, M. (2001). Crack edge element of three-dimensional displacement discontinuity method with boundary division into triangular leaf elements. *Communications in numerical methods in engineering*, 17(6):365–378.

Marshall, S. T. and Morris, A. C. (2012). Mechanics, slip behavior, and seismic potential of corrugated dip-slip faults. *Journal of Geophysical Research: Solid Earth*, 117(B3).

Martel, S. J. and Muller, J. R. (2000). A two-dimensional boundary element method for calculating elastic gravitational stresses in slopes. *Pure and Applied Geophysics*, 157(6-8):989–1007.

Meng, C., Maerten, F., and Pollard, D. D. (2013). Modeling mixed-mode fracture propagation in isotropic elastic three dimensional solid. *International Journal of Fracture*, 179(1-2):45–57.

Mildren, S., Hillis, R., and Kaldi, J. (2002). Calibrating predictions of fault seal reactivation in the timor sea. *The APPEA Journal*, 42(1):187–202.

Niebe, S. and Erleben, K. (2015). Numerical methods for linear complementarity problems in physics-based animation. *Synthesis Lectures on Computer Graphics and Animation*, 7(1):1–159.

Niebe, S. M. (2009). Pain and agony using a newton based method.

Nikkhoo, M. and Walter, T. R. (2015). Triangular dislocation: an analytical, artefact-free solution. *Geophysical Journal International*, 201(2):1119–1141.

Olson, J. and Pollard, D. D. (1989). Inferring paleostresses from natural fracture patterns: A new method. *Geology*, 17(4):345–348.

Olson, J. E. (1991). *Fracture mechanics analysis of joints and veins*. PhD thesis, Stanford University.

Persson, B. N. (2006). Contact mechanics for randomly rough surfaces. *Surface science reports*, 61(4):201–227.

Persson, P.-O. and Strang, G. (2004). A simple mesh generator in matlab. *SIAM review*, 46(2):329–345.

Pollard, D., Bergbauer, S., and Mynatt, I. (2004). Using differential geometry to characterize and analyse the morphology of joints. *Geological Society, London, Special Publications*, 231(1):153–182.

Pollard, D. and Fletcher, R. C. (2005). *Fundamentals of structural geology*. Cambridge University Press.

Pollard, D. and Segall, P. (1987). Pollard, david d., and paul segall. "theoretical displacements and stresses near fractures in rock: with applications to faults, joints, veins, dikes, and solution surfaces. In Atkinson, B., editor, *Fracture mechanics of rock*, pages 277–374. Academic press, London.

Power, W. and Durham, W. (1997). Topography of natural and artificial fractures in granitic rocks: Implications for studies of rock friction and fluid migration. *International Journal of Rock Mechanics and Mining Sciences*, 34(6):979–989.

Renard, F., Mair, K., and Gundersen, O. (2012). Surface roughness evolution on experimentally simulated faults. *Journal of Structural Geology*, 45:101–112.

Resor, P. G. and Meer, V. E. (2009). Slip heterogeneity on a corrugated fault. *Earth and Planetary Science Letters*, 288(3-4):483–491.

Ritz, E., Mutlu, O., and Pollard, D. D. (2012). Integrating complementarity into the 2d displacement discontinuity boundary element method to model faults and fractures with frictional contact properties. *Computers & geosciences*, 45:304–312.

Ritz, E. and Pollard, D. D. (2012). Stick, slip, and opening of wavy frictional faults: A numerical approach in two dimensions. *Journal of Geophysical Research: Solid Earth*, 117(B3).

Ritz, E., Pollard, D. D., and Ferris, M. (2015). The influence of fault geometry on small strike-slip fault mechanics. *Journal of Structural Geology*, 73:49–63.

Roberts, G. P. and Ganas, A. (2000). Fault-slip directions in central and southern greece measured from striated and corrugated fault planes: Comparison with focal mechanism and geodetic data. *Journal of Geophysical Research: Solid Earth*, 105(B10):23443–23462.

Sagy, A., Brodsky, E. E., and Axen, G. J. (2007). Evolution of fault-surface roughness with slip. *Geology*, 35(3):283–286.

Sheibani, F., Olson, J., et al. (2013). Stress intensity factor determination for three-dimensional crack using the displacement discontinuity method with applications to hydraulic fracture height growth and non-planar propagation paths. In *ISRM International Conference for Effective and Sustainable Hydraulic Fracturing*. International Society for Rock Mechanics and Rock Engineering.

Tada, H., Paris, P. C., Irwin, G. R., and Tada, H. (2000). *The stress analysis of cracks handbook*, volume 130. ASME press New York.

Thomas, A. L. and Pollard, D. D. (1993). The geometry of echelon fractures in rock: implications from laboratory

and numerical experiments. *Journal of Structural Geology*, 15(3-5):323–334.

Willemse, E. J. (1997). Segmented normal faults: Correspondence between three-dimensional mechanical models and field data. *Journal of Geophysical Research: Solid Earth*, 102(B1):675–692.

Yang, S., Jiang, Y., Xu, W., and Chen, X. (2008). Experimental investigation on strength and failure behavior of pre-cracked marble under conventional triaxial compression. *International Journal of Solids and Structures*, 45(17):4796–4819.

FIGURE CAPTIONS

EarthArXiv postprint, accepted for publication in the Journal of Structural Geology -
https://doi.org/10.1016/j.jsg.2018.11.009

Figure 1: Geometry and boundary conditions of the elastic boundary-value problem of a line and penny-shaped crack subject to uniform shear or tensile loads. Traction directions are relative to the fractures normal (n) and Θ is the angle away from the direction of shearing. The crack surfaces have been artificially separated (grey area) in order to see its faces and the respective tractions acting on these.

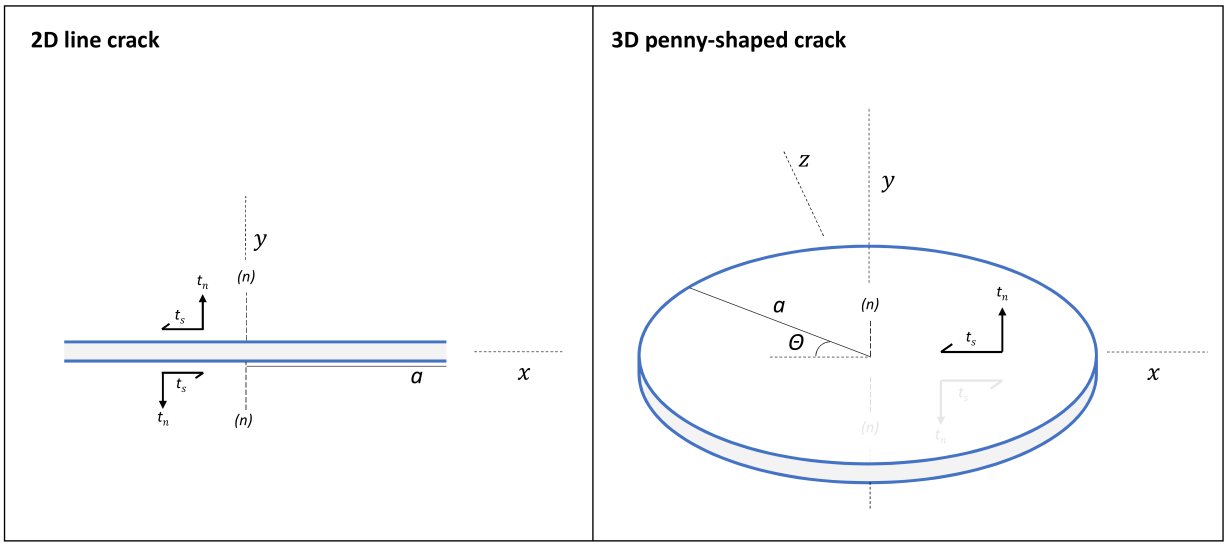

EarthArXiv postprint, accepted for publication in the Journal of Structural Geology -
https://doi.org/10.1016/j.jsg.2018.11.009

Figure 2: Positive displacement and traction component convention adopted for the 3D DDM formulation. Traction and discontinuity convention match, positive D_n and t_n are opening and tension respectively. In the xy-plane positive D_{ss} and t_{ss} are left lateral, i.e. along the direction counter-clockwise from the element normal (n). For D_{ds} and t_{ds} positive directions are those where the angle between the normal and the shear direction in question (ϕ) contains the z-axis. For flat triangles the convention of Nikkhoo and Walter (2015) is used, for normal vectors facing upwards, D_{ss} and D_{ds} are positive when shearing south and west, whereas when the normal vector points downward, positive directions face north and west.

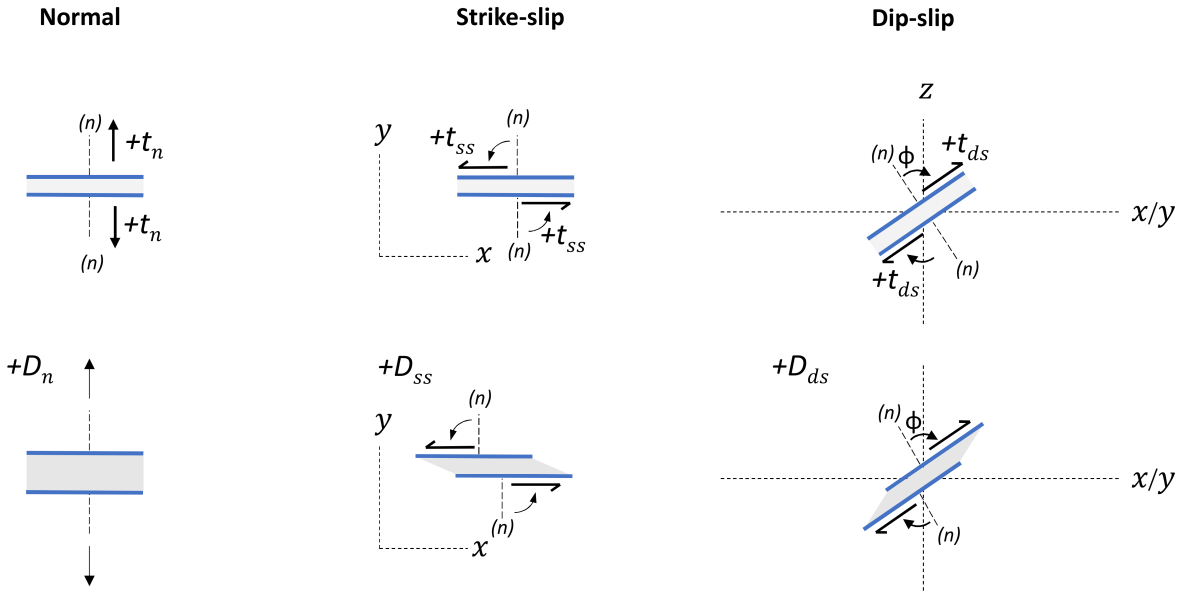

EarthArXiv postprint, accepted for publication in the Journal of Structural Geology -
https://doi.org/10.1016/j.jsg.2018.11.009

Figure 3: A summary of the 3D friction cone used in the numerical calculation. Figure adapted from Kaven et al. (2012); Niebe (2009)

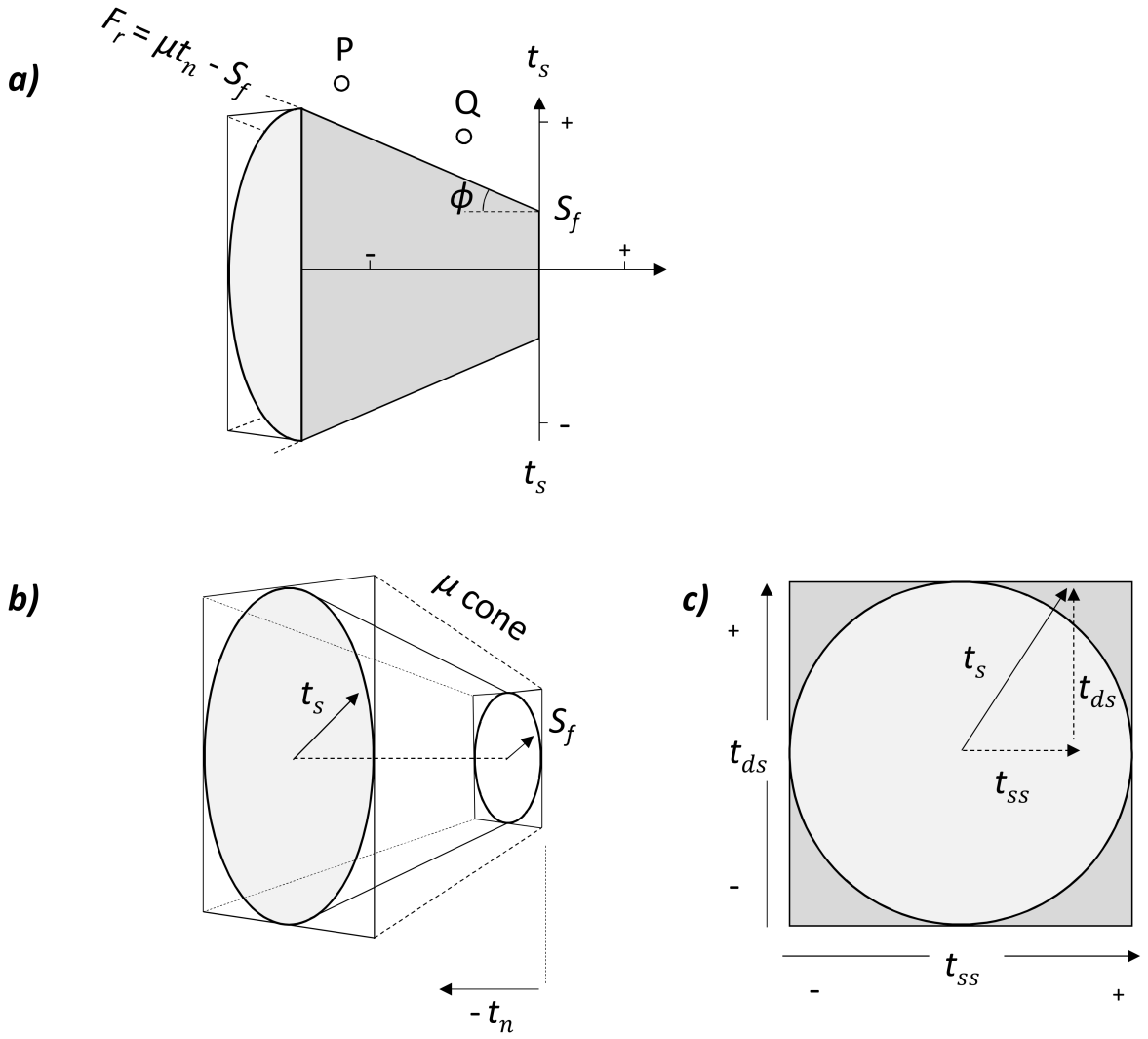

EarthArXiv postprint, accepted for publication in the Journal of Structural Geology -
https://doi.org/10.1016/j.jsg.2018.11.009

Figure 4: Benchmarking of the numerical results against analytical solutions. D_s represents the slip of the penny-shaped crack normalised to the maximum slip value from 2. The sampling used is described in the text. c) shows the crack tip elements overestimation of the analytical slip profile in percent vs Θ.

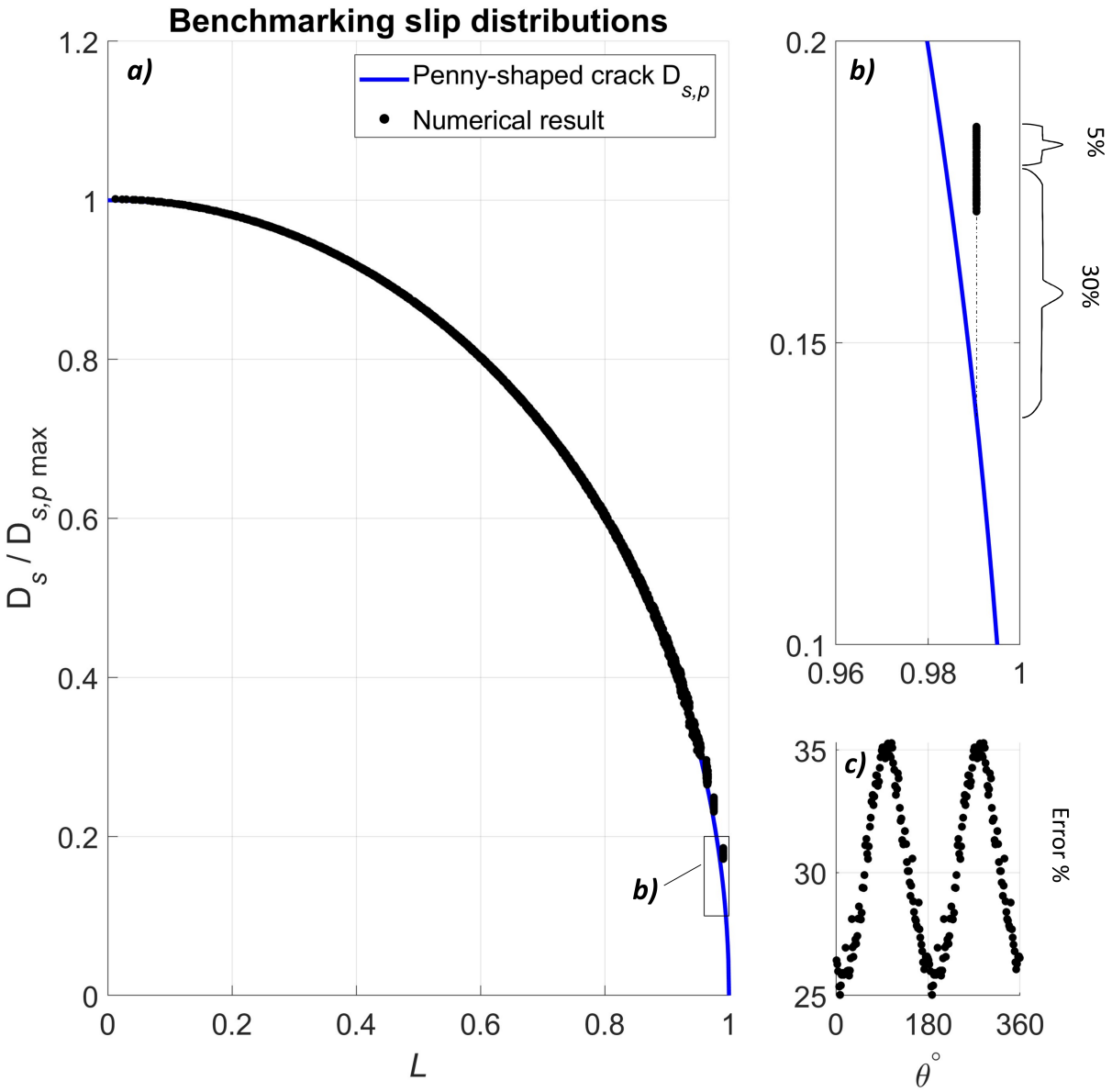

EarthArXiv postprint, accepted for publication in the Journal of Structural Geology -
https://doi.org/10.1016/j.jsg.2018.11.009

Figure 5: a) Boundary conditions used in the numerical analysis that lie in the xy-plane. λ is the wavelength and the amplitude is H. b) Slip direction (white arrow) perpendicular corrugations. c) Slip direction parallel with corrugations. Note that the dashed boundaries are included to highlight the principal stress directions, the fracture surfaces modelled lie within an infinite elastic medium.

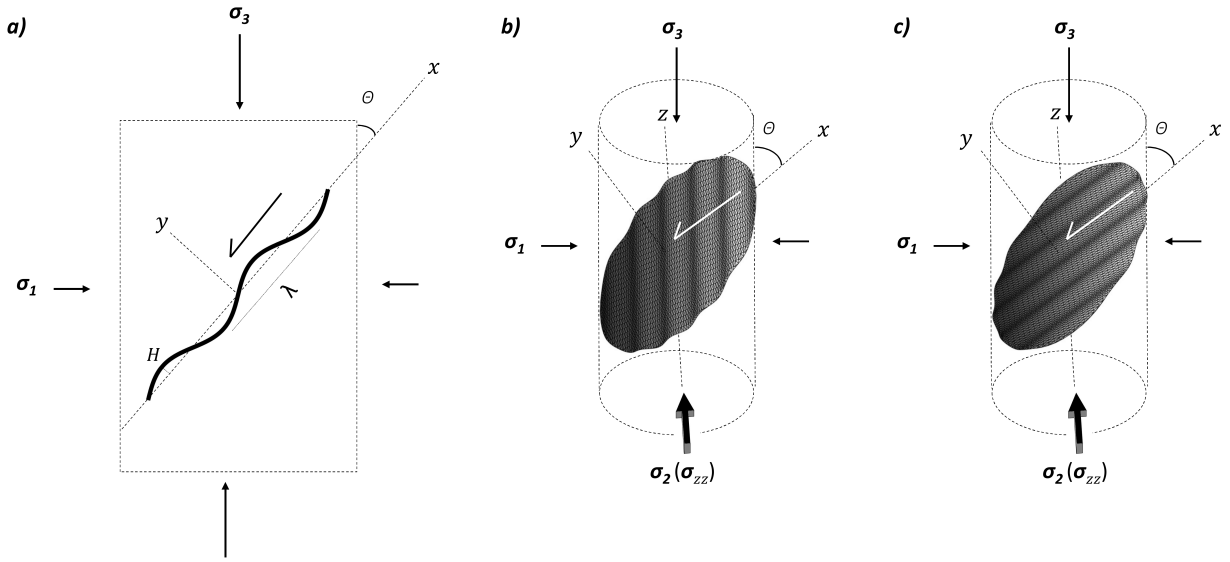

EarthArXiv postprint, accepted for publication in the Journal of Structural Geology -
https://doi.org/10.1016/j.jsg.2018.11.009

Figure 6: Cross section through 3D slip distributions for a planar and wavy fault. Here a=1 and the xz axes of the graph are the location on the cracks walls. The wavy fault has an H and λ that are 2% and 37.5% of a respectively. D_s here is slip normalised to a planar faults maximum slip value from Eq. 2.

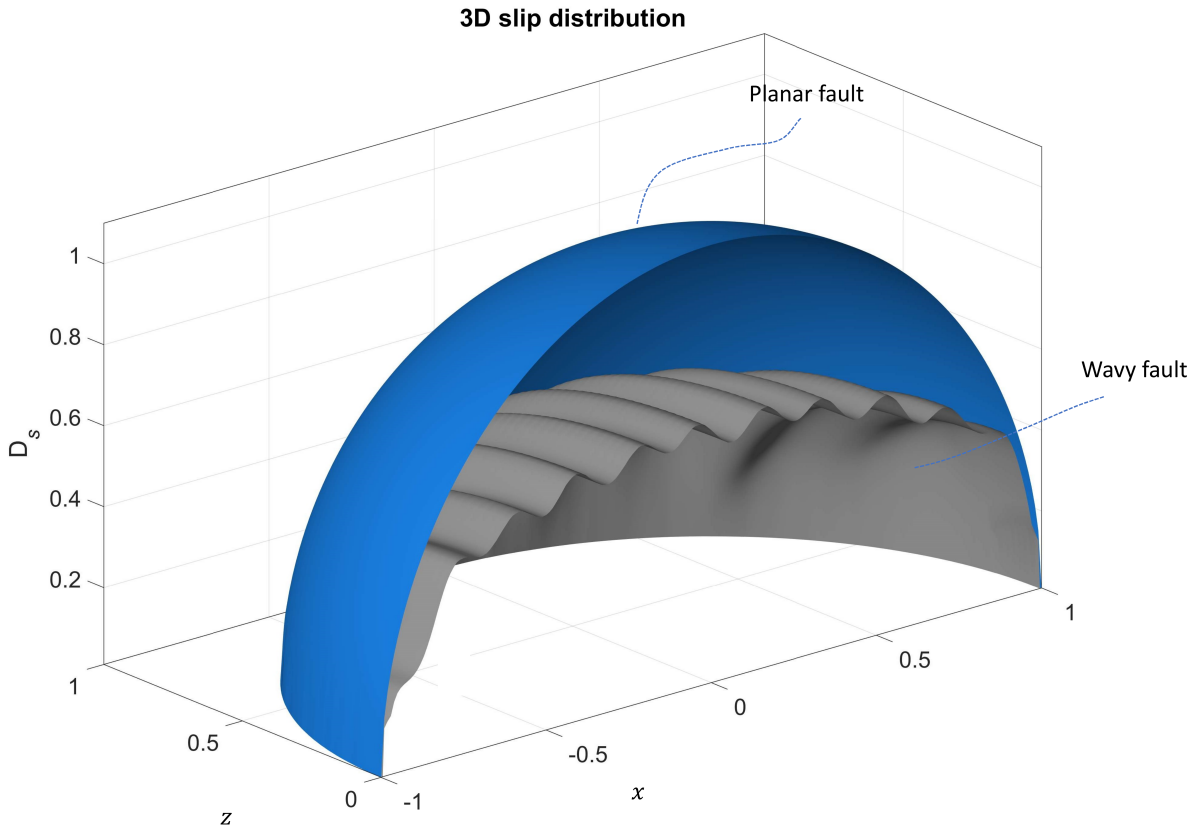

Figure 7: Stress intensity factor approximation using the 3D DDM method. Analytical curves shown are for a penny-shaped crack subject to shear stress; Eq. 24. All results are normalised the maximum analytical value of K_{II}. The numerical approximation is shown as dots. The sampling used, and boundary conditions on the fracture are those described in the benchmarking section. The signs here follow the shear direction convention shown in Figure 9.30 of Pollard and Fletcher (2005). The positive direction of the crack y-axis in Fig. 5b corresponds to the y-axis in the local coordinate system of their figure.

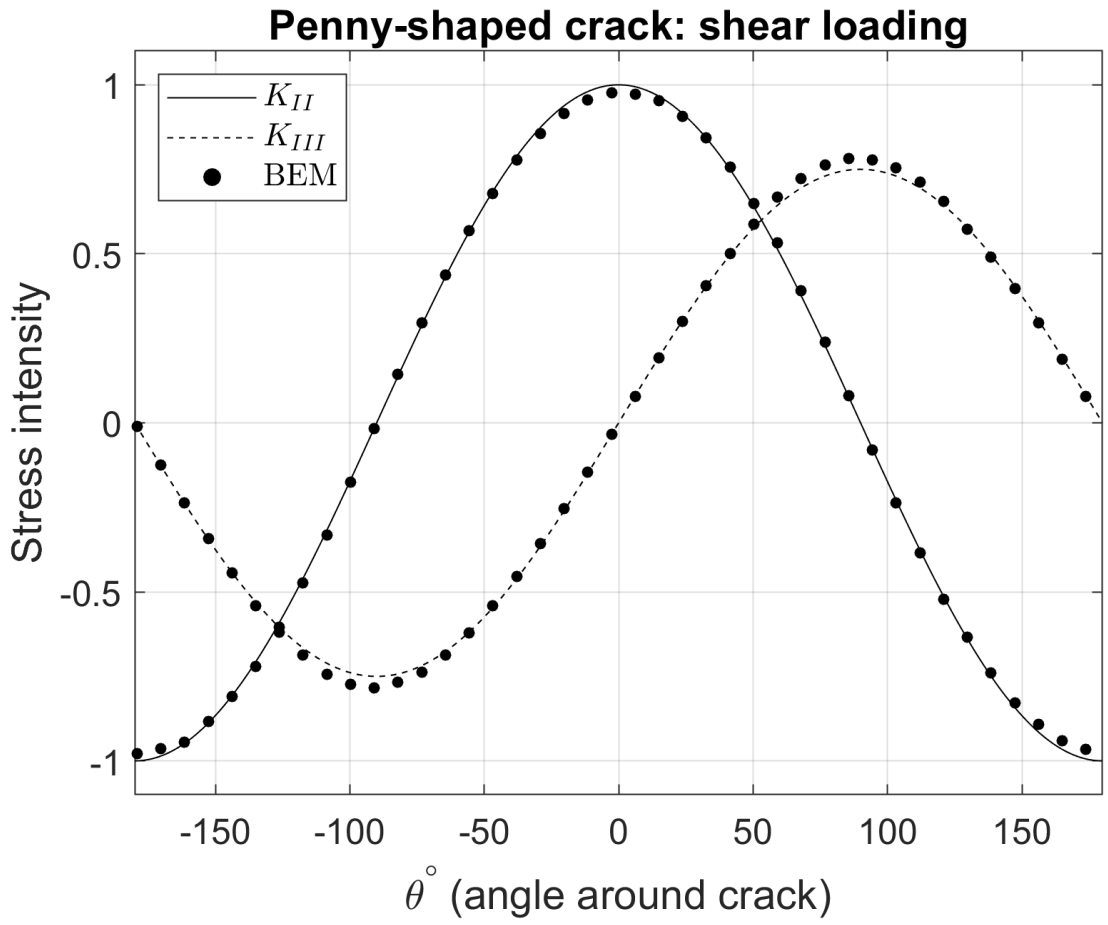

EarthArXiv postprint, accepted for publication in the Journal of Structural Geology -
https://doi.org/10.1016/j.jsg.2018.11.009

Figure 8: Comparison between numerical results for 2D (A) and 3D (V) slip reduction due to changes in a wavy fault surfaces amplitude and wavelength. Squares are the resultant 2D slip area and diamonds are the 3D slip volume. Results on the y-axis are relative to Eqs. 3 and 4. Different colours on the graph correspond to different wavelengths relative to half-length a. On the right of the figure we show our mesh captures the most extreme waveform we show this looking down the corrugations for a waveform where H and λ are 3.5% and 25% of a respectively. The slight deviations at the wave crests are caused by the added equilateral edge triangles.

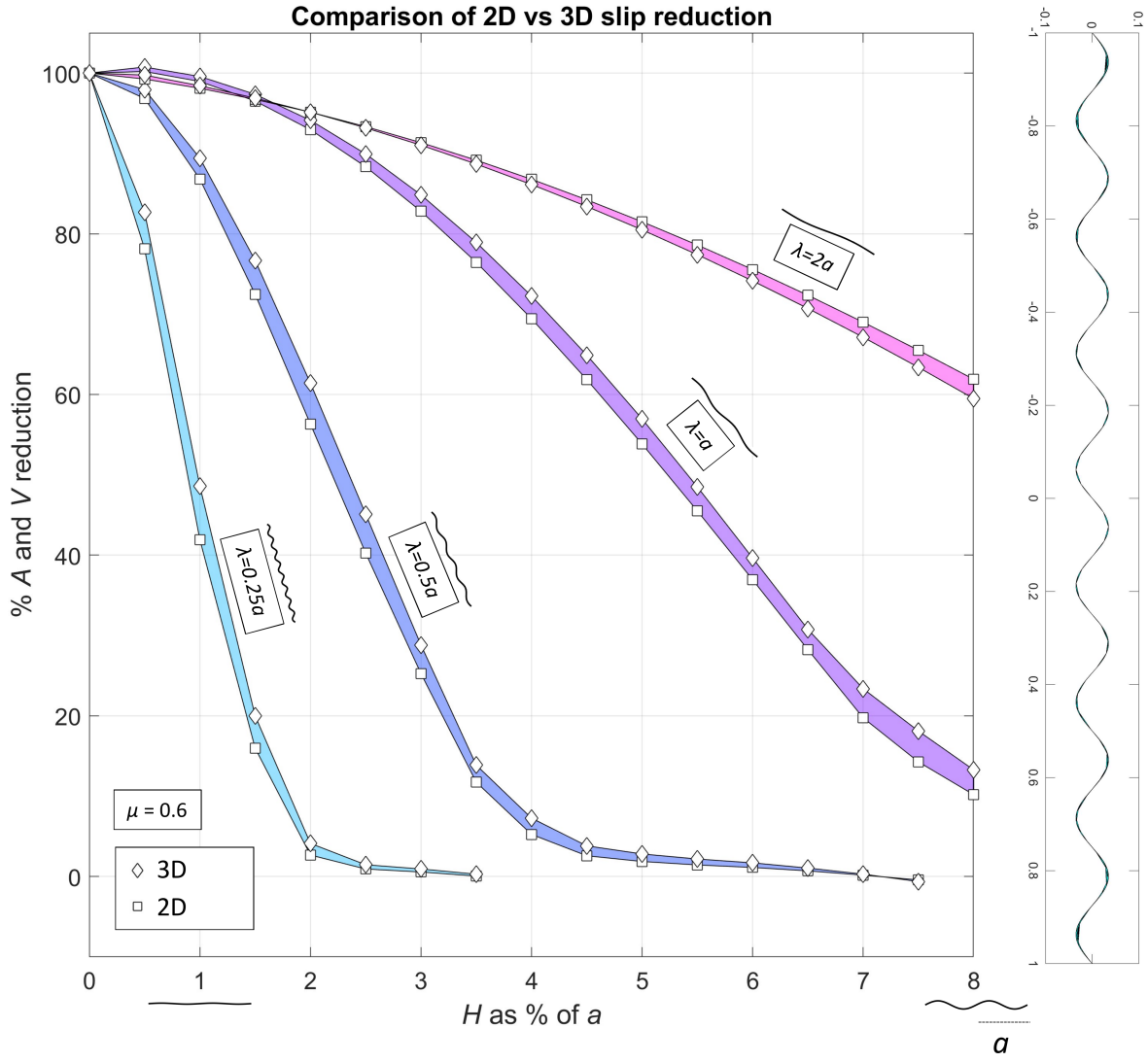

EarthArXiv postprint, accepted for publication in the Journal of Structural Geology -
https://doi.org/10.1016/j.jsg.2018.11.009

Figure 9: Deformation pattern of the fracture walls when slip is perpendicular (top) and parallel (bottom) to corrugations. The dotted line represents the fractures boundary. The light uniformly gridded squares in the background represent one of the fracture walls before deformation. The deformed grid is the resultant displacement once this wall shears. The topography of the surface is shown as the 2D lines at the side; this waveform corresponds to an H and λ that are 4% and 75% of a respectively. Boundary conditions are as stated but the displacement is exaggerated by 300 times. xz-axes correspond to those shown in Fig. 5b) and c). σ_{zz} here has been set equal to σ_{xx}.

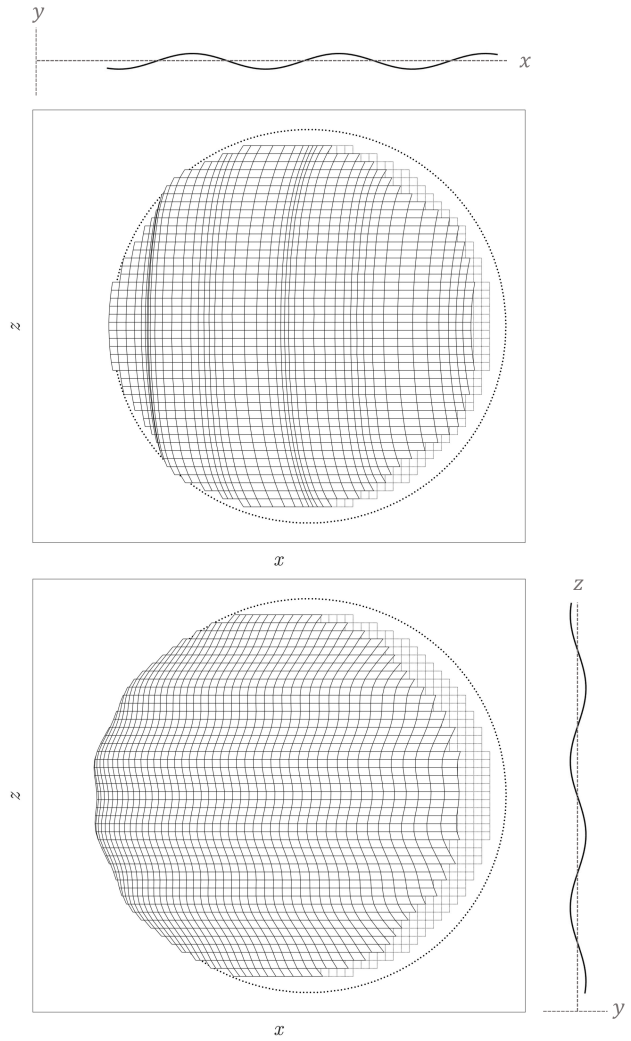

EarthArXiv postprint, accepted for publication in the Journal of Structural Geology -
https://doi.org/10.1016/j.jsg.2018.11.009

Figure 10: 3D slip V reduction due to changes in a wavy fault surfaces amplitude and wavelength. Diamonds are when slip is perpendicular with corrugations and squares parallel. Note perpendicular results match those in Fig. 8. Results on the y-axis are relative to a planar fault described by Eq. 4. Different colours on the graph correspond to different wavelengths relative to half-length a.

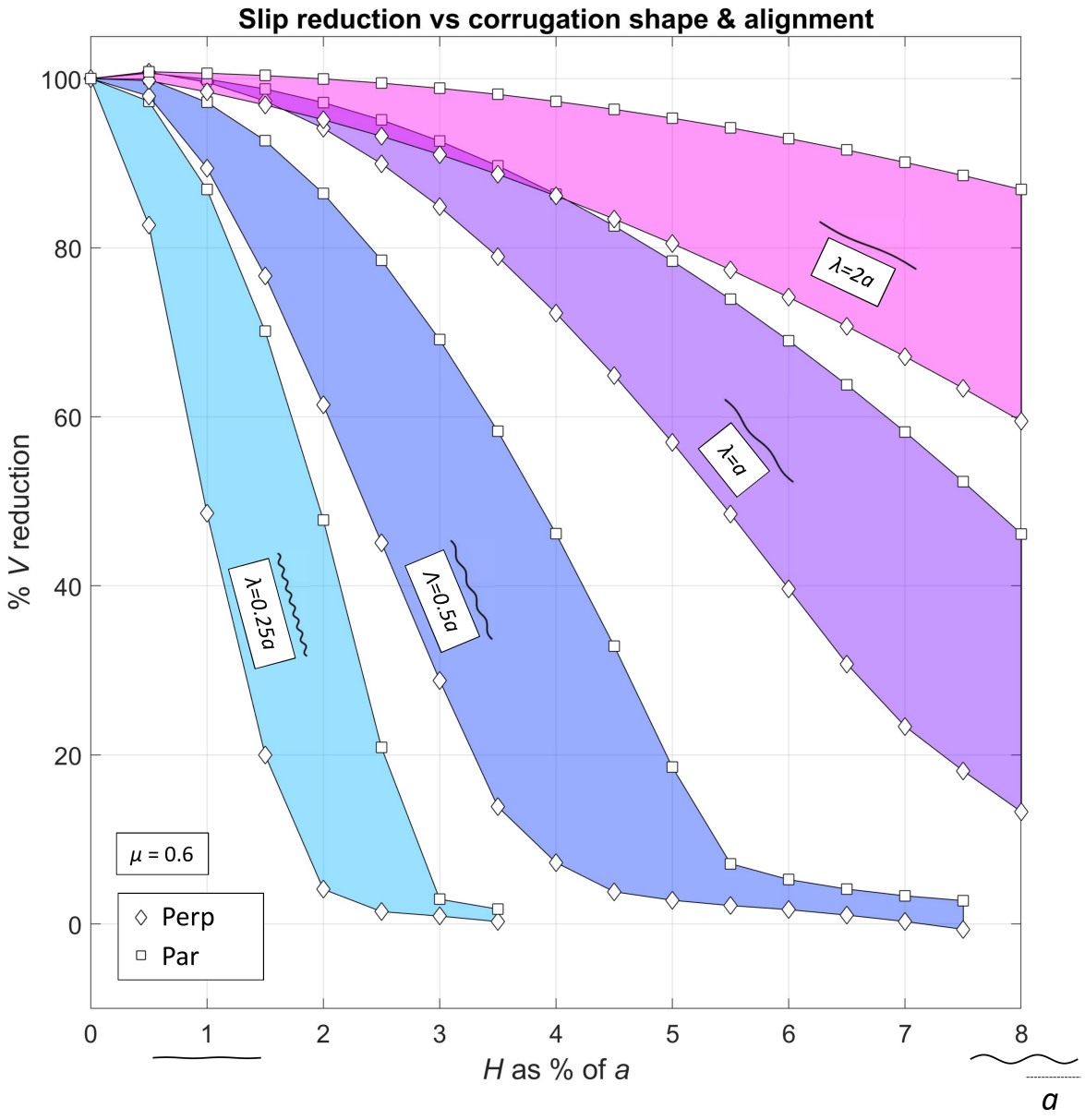

EarthArXiv postprint, accepted for publication in the Journal of Structural Geology -
https://doi.org/10.1016/j.jsg.2018.11.009

Figure 11: 3D slip V reduction due to changes in a wavy fault surfaces amplitude and wavelength. Diamonds are when the stress out of the plane of shearing is low (equal to σ_{yy}) and squares when this is high (equal to σ_{xx}). Results on the y- axis are relative to a planar fault described by Eq. 4. Different colours on the graph correspond to different wavelengths relative to half-length a. Values of μ shown on the right of y-axis are adjusted coefficients of friction for planar faults, these will reduce the slip volume by the amount shown on the left y-axis (relative to the volume when μ is 0.6).

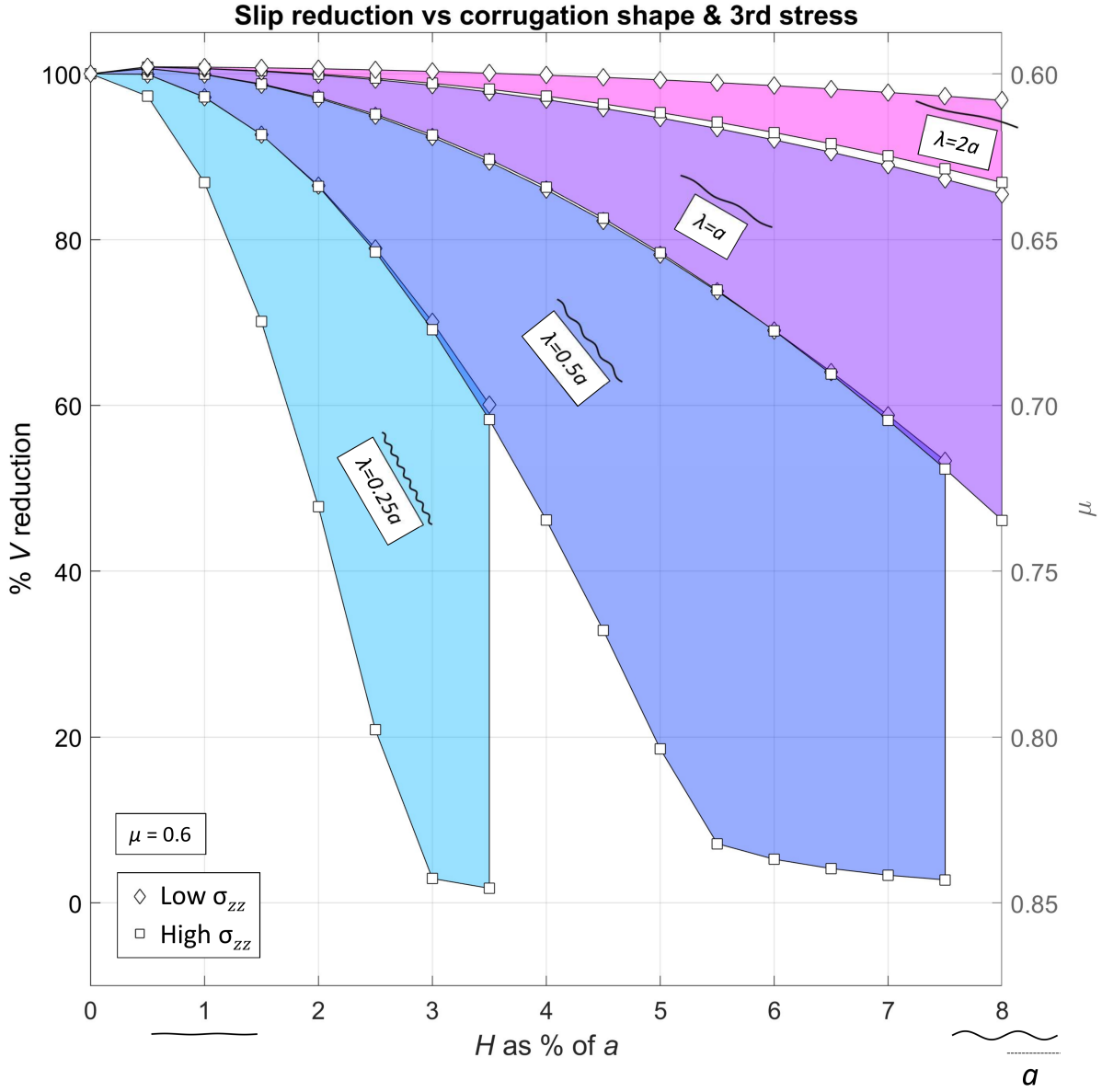

EarthArXiv postprint, accepted for publication in the Journal of Structural Geology -
https://doi.org/10.1016/j.jsg.2018.11.009

Figure 12: Stress intensity factor reductions due to corrugations, comparison between 2D and 3D results. Results on the y-axis are relative to a planar fault described by Eq. 24. Different colours on the graph correspond to different wavelengths relative to half-length a.

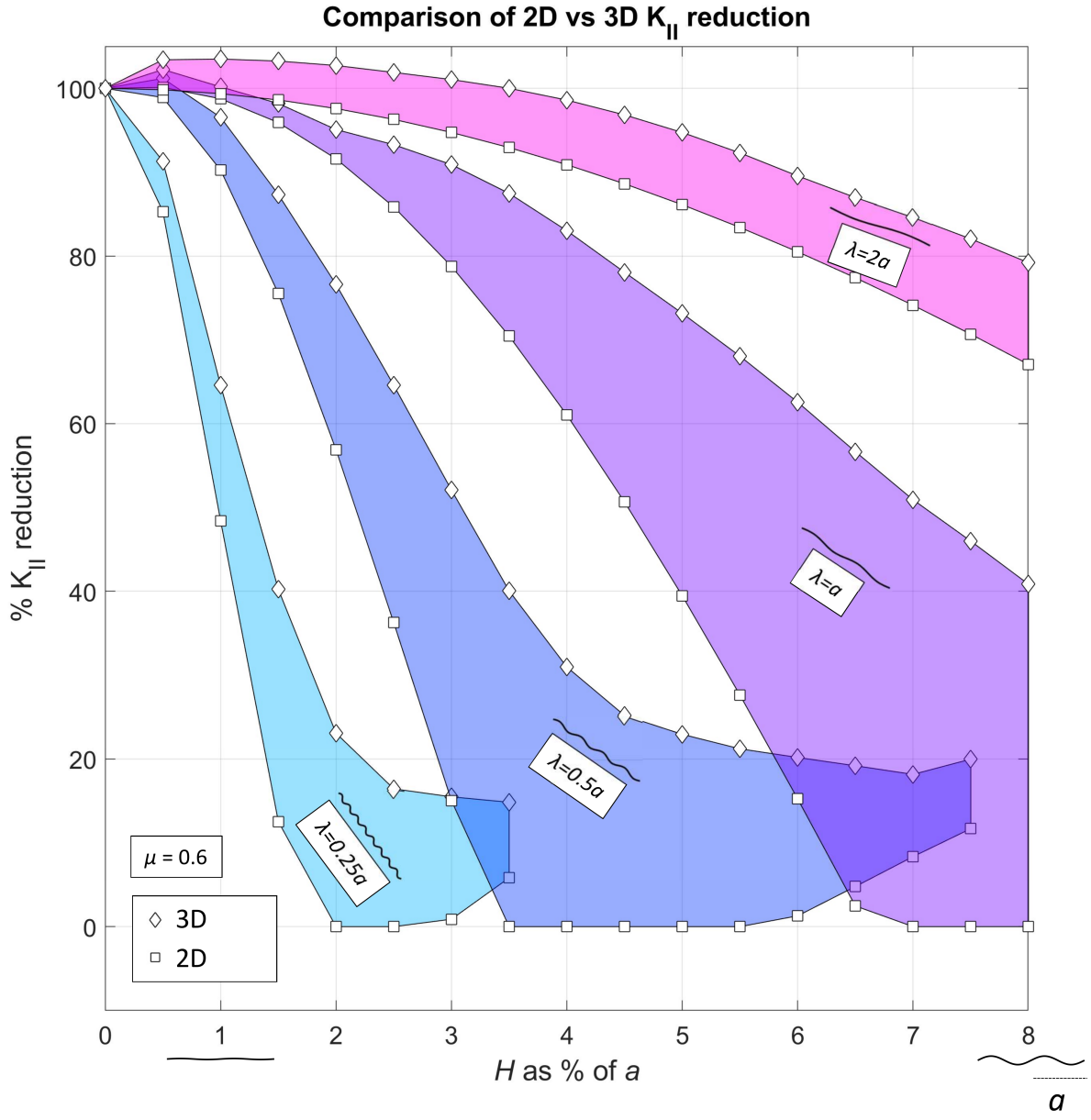

Figure 13: Waveform and associated lenticular opening apertures on the fault surface. Results scaled relative to Eq. 26.

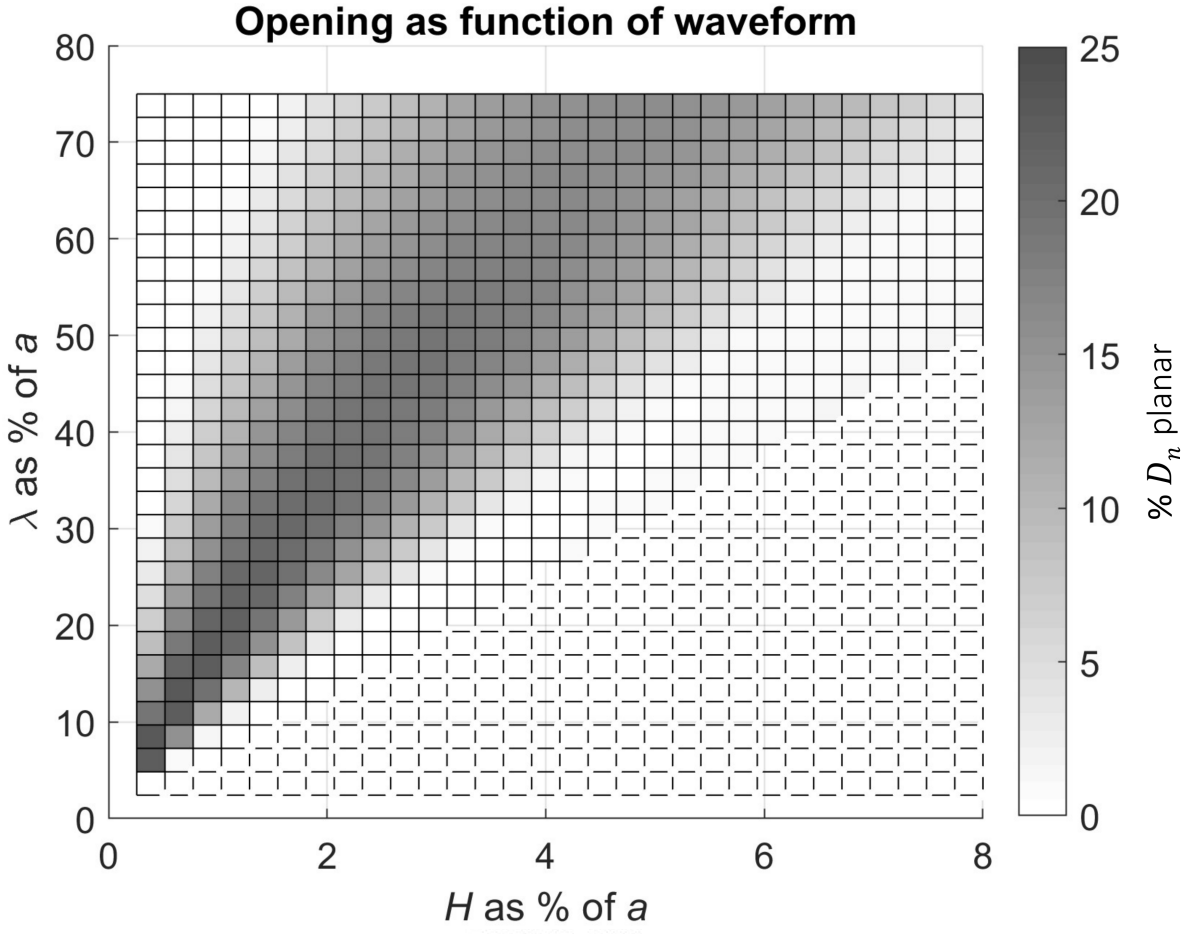

EarthArXiv postprint, accepted for publication in the Journal of Structural Geology -
https://doi.org/10.1016/j.jsg.2018.11.009

Figure 14: a) 2D fracture profile from Ritz et al. (2015), Fig.8, fracture is approximately 3 m long. b) 2D approximation with waveform: $\lambda = a$, $H = 2.5\%$ of a. c) 3D fracture surface from photogrammetry on a sandstone block (self-defined edges), the exposed fracture surface was 2 m wide, looking into the x-axis (slip direction). The height of the surface in the y-axis varies by 14 cm. d) Approximation of c) with the waveform: $\lambda = 200\%$ of a, $H = 5\%$ of a. e) 3D fracture surface front coloured for height/depth away from 0. f) 3D fracture surface front approximation of d) with the same colour scale as e).

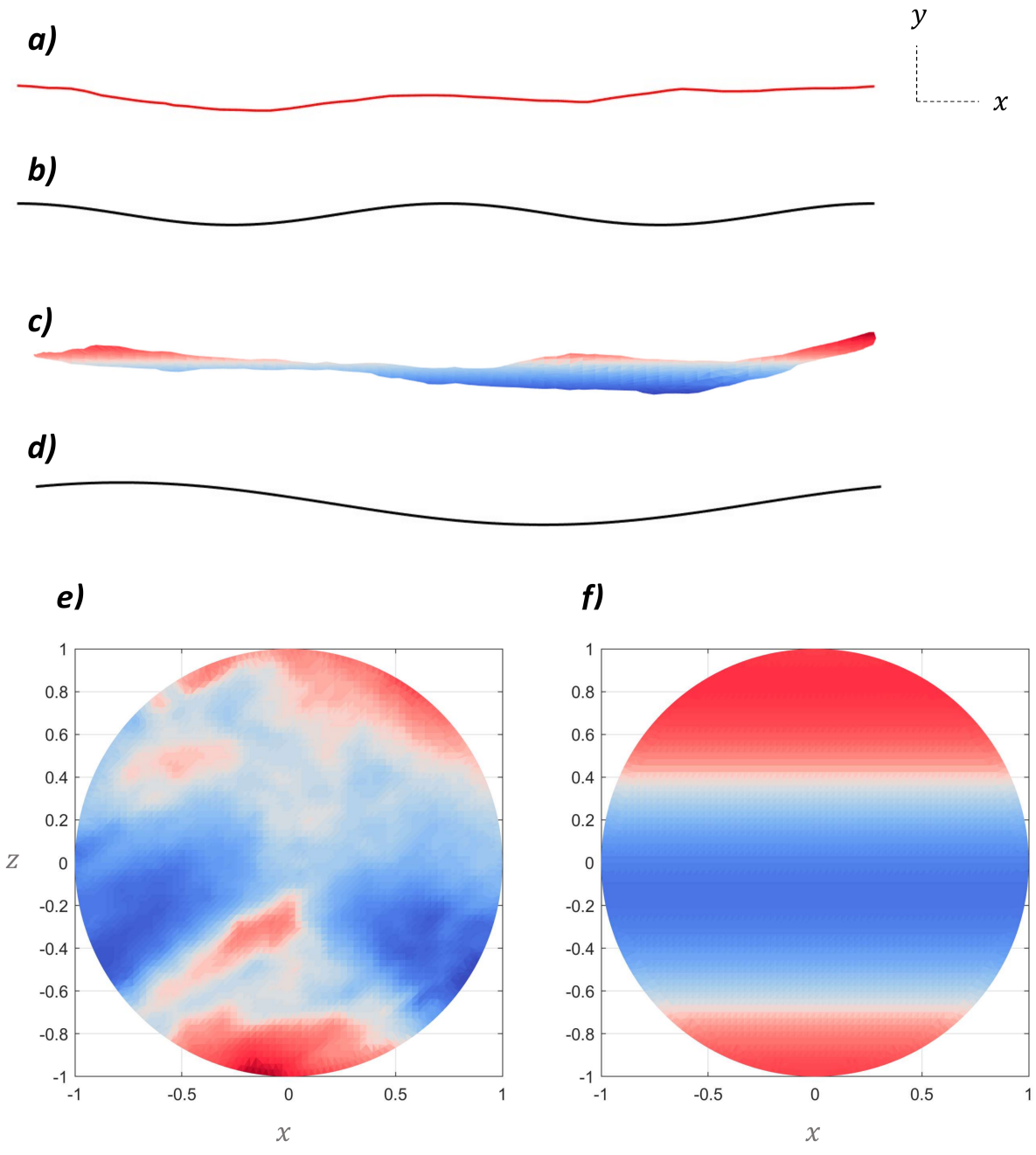

Figure 15: Comparison between crack wall displacements for a penny-shaped crack and an approximation of displacements close to the tip for a fracture a 10th of the length.

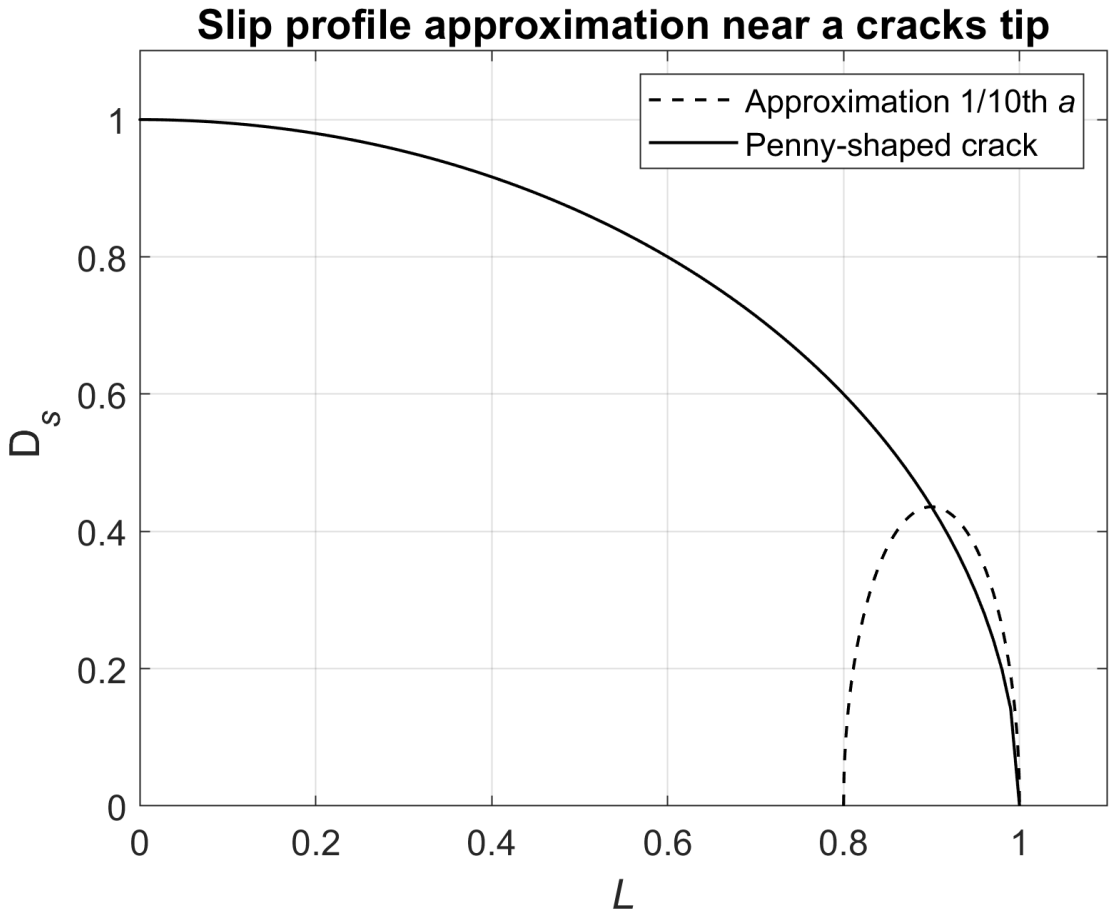

EarthArXiv postprint, accepted for publication in the Journal of Structural Geology -
https://doi.org/10.1016/j.jsg.2018.11.009

Figure 16: The resulting stress intensity error for multiple meshes, compared to analytical solutions for an inclined penny shaped crack subject to tension. ν was set to 0.25 for all runs. The maximum and minimum errors are shown as solid horizontal lines, mean as shapes. Shades highlight the mode. The mean error shown in the y-axis is the sum of residuals r divided by the number of edge triangles n divided by the maximum value of the stress intensity in question for this geometry. The x-axis shows the mean mesh quality, defined as two times the radius of the triangles inscribed circle to the radius of its circumscribed circle. A value of one is a mesh where all triangles are equilateral, some examples triangles are shown below their respective values. Mesh sizes (number of triangles) are shown above each data point.

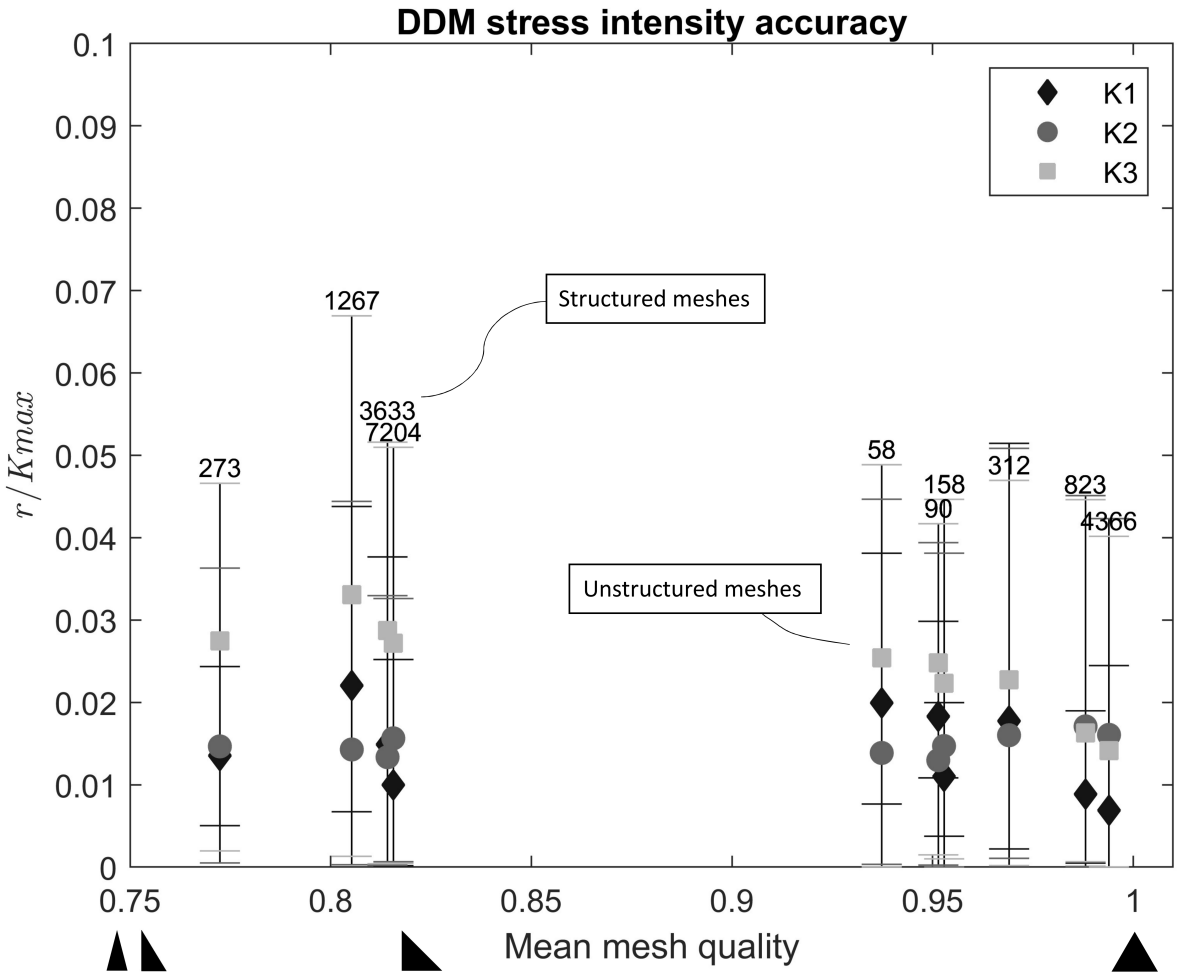

Figure 17: The lowest and highest density meshes used in Fig.16. The text describes the number of triangles. The mesh used in the bottom left is the mesh used in this study.